

Clustering effects on the Dark Siren determination of H_0 : A simulation study

Marios Kalomenopoulos^{1,3*} , Riccardo Barbieri², Sadegh Khochfar¹, Jonathan Gair², Robert J. McGibbon^{1,4}

¹*Institute for Astronomy, University of Edinburgh, Royal Observatory, Edinburgh EH9 3HJ, UK*

²*Max Planck Institute for Gravitational Physics, Potsdam Science Park, Am Mühlenberg 1, D-14476 Potsdam, Germany*

³*Department of Physics and Astronomy, University of Nevada, Las Vegas, NV 89154, USA*

⁴*Leiden Observatory, Leiden University, PO Box 9513, 2300 RA Leiden, The Netherlands*

Accepted XXX. Received YYY; in original form ZZZ

ABSTRACT

Gravitational waves (GWs) offer an alternative way to measure the Hubble parameter. The optimal technique, the “bright siren” approach, requires the identification of an electromagnetic counterpart. However, a significant fraction of gravitational waves signals will not have counterparts. Such events can still constrain the Hubble parameter H_0 via statistical methods, exploiting galaxy information from the GWs sky localisation volume. In this work, we investigate the power of this method using high-resolution, cosmological simulations that include realistic clustering. We find that clustering leads to increased convergence of the H_0 posteriors, with clear recovery of the input value as early as $N_{\text{gw}} = 40$ events, compared to uniform catalogues, where the posterior remains largely unconstrained, even with $N_{\text{gw}} = 100$ events.

In addition, we quantify the role of catalogue incompleteness. We show that catalogues with completeness levels as low as $f = 25\%$ can be competitive with fully complete catalogues, confirming the impact of clustering. Completeness levels of $f = 50\%$ perform statistically similar to complete catalogues with as few as $N_{\text{gw}} = 40$ events. This indicates the need to focus on improving gravitational waves detection capabilities, rather than obtaining more complete galaxy catalogues.

Finally, we investigate additional properties of the method by taking into consideration physical weights, different observational errors, potential biases from the H_0 priors, a variety of detectors’ horizon distances, and different methods of catalogue completion and statistical analysis.

Key words: cosmology: large-scale structure of the Universe – cosmological parameters – gravitational waves

1 INTRODUCTION

One of the basic parameters of the standard cosmological model is the Hubble-Lemaître parameter (Hubble 1929; Lemaître 1931), which describes the expansion speed of our universe (Friedmann 1922). There is a long history of dedicated observations that try to measure it, and more specifically its value at the present time H_0 (Freedman & Madore 2010; Jackson 2015; Steer 2020; Freedman 2021). However, although the improvement of measurements have constrained H_0 to around 70 km/s/Mpc, the parallel shrinkage of observational errors has led to statistically significant discrepancies among different probes, especially between “early universe” values of $H_0 \simeq 67$ km/s/Mpc (Cuceu et al. 2019; Aghanim et al. 2020)

and “late universe” ones with $H_0 \simeq 73$ km/s/Mpc (Wong et al. 2020; Riess et al. 2019, 2022; H0DN Collaboration et al. 2025).

Even though many possible solutions have been proposed (for a review of measurements and proposed solutions to the current tensions see Di Valentino et al. (2021)), it is certain that more, independent, and complementary measurements need to be made to disentangle between the need of new physics and the potential of missing underlying systematic effects. A very promising and independent technique to measure the Hubble parameter is the use of gravitational wave observations (Schutz 1986; Holz & Hughes 2005; Palmese & Mastrogianni 2025; Poggiani 2025). Contrary to other methods, GWs give direct information about the distance of the source, while in most other approaches this information is subject to larger uncertainties. At the same time, the redshift of the source is not guaranteed, and hard to obtain for most events.

* E-mail: marios.kalomenopoulos@[gmail.com][unlv.edu]

The cleanest technique, a “bright siren”, requires an elec-

tromagnetic (EM) counterpart and was performed for the first time in Abbott et al. (2017b) using the binary neutron star (BNS) merger event GW170817 (Abbott et al. 2017a), giving $H_0 = 70_{-8}^{+12}$ km/s/Mpc¹. Improved constraints of the inclination of the binary (Hotokezaka et al. 2019) reduced the errors to $H_0 = 68.9_{-4.6}^{+4.7}$ km/s/Mpc. Of course, with only one GW observation with an EM counterpart, the uncertainties are still large. At the same time, the detection of a counterpart is difficult, and for the majority of GW events none is expected². Furthermore, cosmological model-dependent biases can pose further complications (Shafieloo et al. 2020). For this reason, a number of other methods have been proposed to get independent information about the redshift.

One is based on exploiting prior knowledge about the population of the sources (Taylor et al. 2012). The GW signals contain information about the redshifted “chirp mass” $M_c = (1+z)M_c$, where $M_c = (m_1 m_2)^{3/5} / (m_1 + m_2)^{1/5}$ is the chirp mass of the system in the source frame and m_1, m_2 the masses of the members of the binary. Including prior information about the source M_c and measuring M_c can statistically put constraints on the redshift and hence on H_0 . For more details on this technique, we refer to Mastroianni et al. (2021). Based on the GW observations until the end of O3, the third LIGO-Virgo-KAGRA (LVK) observing run (Tse et al. 2019; Acernese et al. 2019; Buikema et al. 2020; Acernese et al. 2023; Abbott et al. 2023a, 2024), this method gave a value of the Hubble parameter $H_0 = 50_{-30.0}^{+37.0}$ km/s/Mpc (Abbott et al. 2023b), while after the first part of the fourth observing run (GWTC-4.0) (LIGO Scientific Collaboration et al. 2015; Acernese et al. 2015; Akutsu et al. 2021; Capote et al. 2025; Soni et al. 2025; The LIGO Scientific Collaboration et al. 2025a), the “spectral siren” result was $H_0 = 112.7_{-35.9}^{+51.0}$ km/s/Mpc (The LIGO Scientific Collaboration et al. 2025c). Both results correspond to the choice of a POWER LAW + PEAK model for the underlying mass distribution. A more realistic mass model, FULLPOP-4.0 (The LIGO Scientific Collaboration et al. 2025b), yields $H_0 = 76.4_{-18.1}^{+23.0}$ km/s/Mpc for GWTC-4.0 (The LIGO Scientific Collaboration et al. 2025c).

Finally, another method to get information about the redshifts is the “dark sirens” technique, where with “dark” we refer to GWs observations without an EM counterpart (see Gair et al. (2022) for a pedagogical introduction to the method). It was first proposed in Schutz (1986) and the basic idea consists of using all the galaxies in the GW sky localisation volume as potential hosts, and statistically compute the H_0 parameter.

Although this method can also be used for individual observations: GW170817 (Fishbach et al. 2019), GW170814 (Soares-Santos et al. 2019), GW190814 (Abbott et al. 2020; Palmese et al. 2020), its real strength comes from combining multiple events, assumed to be independent from each other.

Statistical determinations of H_0 have been performed with GW observations of the first three observing runs and the first part of the fourth observing run: using observations up until the end of O2 & GW170817 (Abbott et al. 2019, 2021a,b,c), giving $H_0 = 68.7_{-7.8}^{+17}$ km/s/Mpc, using only observations up until the end of O2 (Finke et al. 2021), giving $H_0 = 67.3_{-17.9}^{+27.6}$ km/s/Mpc, using events observed up until the end of O3 (Abbott et al. 2023a), together with a BBH population model and GLADE+ galaxy cata-

logue (Dálya et al. 2018, 2022) giving $H_0 = 67.0_{-12.0}^{+13.0}$ km/s/Mpc (Abbott et al. 2023b), or $H_0 = 79.8_{-12.8}^{+19.1}$ km/s/Mpc (Palmese et al. 2023) using the Dark Energy Spectroscopic Instrument (DESI) (DESI Collaboration et al. 2016) and the Dark Energy Survey (DES) (The Dark Energy Survey Collaboration 2005), and finally, till the first part of O4, giving $H_0 = 81.6_{-15.9}^{+21.5}$ km/s/Mpc, using the updated FULLPOP-4.0 population model and GLADE+ (The LIGO Scientific Collaboration et al. 2025c).

Still, this technique is in its infancy, with only a few GW sources statistically informative for a “dark sirens” H_0 study³. For this reason, the power of the method is under active research, with improved codes developed that combine different techniques and include information from the BBH population (Mastroianni et al. 2023; Gray et al. 2023). Investigations of the constraining power of “dark sirens” predicted a $\sim 10\%$ determination of H_0 based on 16_{-14}^{+19} well localised (sky volumes less than 10,000 Mpc³) Binary Black holes (BBH) and a $\sim 6\%$ accuracy from around 100 BNS with no observed counterpart from the future runs of current detectors (Chen et al. 2018). These results assumed a uniform distribution of galaxies in comoving volume and complete galaxy catalogues. These two assumptions have been investigated further in the literature. We discuss the main results below.

The existence of clustering is expected to improve the convergence of the method, since the possible hosts would be closer together. In that case, even if the true host of the GW source is missing from the galaxy survey, the presence of its observed neighbours can rectify its absence. Chen et al. (2018) estimated that the effect of clustering can improve convergence by a factor of ~ 2.5 . Realistic clustering was investigated for the first time in MacLeod & Hogan (2008), who used mock galaxy samples from SDSS DR6. They combined simple, cubical GW localisation areas between redshifts $z = 0.1$ and $z = 0.5$ representing observations of extreme-mass-ratio inspirals (EMRIs) with the future space GW detector, the Laser Interferometer Space Antenna (LISA) (Amaro-Seoane et al. 2017). They found that the cross-correlation of 20 GW events with survey data within the LISA sky localisation, will yield a 1% determination of H_0 . An updated study, but with specific patches of SDSS and sky localisation area (max $\Delta\Omega = 30$ degrees squared) corresponding to current and future ground-based detectors was performed in (Nair et al. 2018), yielding $H_0 = 70.0_{-2.8}^{+2.7}$ km/s/Mpc, hence an error of the order of 4% with $N_{\text{gw}} = 100$ GWs events. Finally, other studies (Bera et al. 2020; Mukherjee et al. 2020, 2021; Ghosh et al. 2024; Ferri et al. 2025) investigated a statistical method to infer H_0 exploiting the clustering information of the GWs sources and nearby galaxies, either by calculating their angular cross-correlation or by combining information from the specific power-spectra respectively. Using this technique with GW events without electromagnetic counterparts from the third GW transient catalogue (GWTC-3.0), results to a median value of $H_0 = 82.4_{-27.0}^{+23.0}$ km/s/Mpc (Mukherjee et al. 2024), while forecasts for the LVK and DESI can reach a measurement of H_0 with precision of $\sim 7\%$, while future, ground based detectors, like Cosmic Explorer (Reitze et al. 2019; Evans et al. 2021) and Einstein Telescope (Maggiore et al. 2020; Branchesi et al. 2023) could reduce this to $\sim 1\%$ (Afroz & Mukherjee 2024). The

¹ Errors indicate everywhere the 68.3% credible interval, unless stated otherwise.

² For BNS, tidal effects can permit a direct redshift measurement (Messenger & Read 2012; Messenger et al. 2014). These effects could be measurable on future GWs detectors, like the Einstein Telescope (Maggiore et al. 2020).

³ “Dark sirens” techniques find also other cosmological applications. For example, they can constrain the cosmic dipole (Chen 2025), they can be used with galaxy clusters instead of individual galaxies (Beirnaert et al. 2025), or without any catalogue, but assuming knowledge of the redshift distribution of the merger rates of binary black holes (Ding et al. 2019; Leandro et al. 2022).

effects of GW bias in the GWs-galaxies cross-correlation method was explored in (Cigarrán Díaz & Mukherjee 2022; Dehghani et al. 2025), showing that it can be constrained together with cosmological parameters and that is connected with astrophysical properties.

The effects of incompleteness, i.e., galaxies missing from a survey due to observational limitations, were analysed in more detail in (Gray et al. 2020), where different fractions of galaxies were missing (fractions of galaxy completeness of 25%, 50%, 75% and 100%). Their mock catalogues were uniform in comoving volume. They quantified the less precise determination of H_0 with increased catalogue incompleteness and concluded that a 4.4% precision on H_0 based on galaxy catalogues is achievable with current detectors, assuming a uniform distribution of sources and 50% completeness from 249 BNS events. Moreover, Turски et al. (2025) studied the influence of the galaxy luminosity function (Schechter 1976), when dealing with incomplete catalogues, emphasising the need for an evolving Schechter function as this impacts the results on H_0 . Finke et al. (2021) investigated the inference of H_0 from “dark sirens” in (Abbott et al. 2021a) together with the GLADE galaxy catalogue (Dálya et al. 2018), where they improved on the statistical analysis of various selection effects, but also in the completeness methodology. For the latter, apart from the uniform completion, they proposed a more realistic model of multiplicative completion, which takes into account the level of clustering of the relevant region compared to the mean density of galaxies in the Universe. More recently, Dalang & Baker (2024); Dalang et al. (2024) developed a method that takes into account clustering information - specifically the variance of galaxy numbers - when dealing with surveys with missing galaxies, while Leyde et al. (2024, 2025) used a Bayesian method for galaxy density and magnitude reconstruction based on large-scale structure information. Lastly, VanWyngarden et al. (2025) investigated how astrophysical information could alleviate the effects of catalogue incompleteness.

In this work, we are interested in investigating further the two scenarios discussed above - effects of clustering & catalogue completeness - within the context of the “dark sirens” statistical technique. We perform this task by exploiting for the first time cosmological N-body simulations combined with galaxy properties provided from machine learning (ML) techniques (McGibbon & Khochfar 2022). This approach will ensure self-consistent clustering information as well as galaxy properties. We investigate the consequences of introducing physical weights, like masses and magnitudes, to individual galaxies when calculating the final posteriors. Our work aims to clarify some of the important intricacies of the “dark sirens” method and contribute to the observational strategies of future GWs observations.

Our paper is structured as follows: In section 2 we introduce our simulations and present our methodology for calculating H_0 , in section 3 we comment on our results on the H_0 posteriors in a clustered environment, with complete and incomplete catalogues and finally, in section 4 we discuss our conclusions and possible extensions.

2 METHODS

2.1 Simulations

To calculate realistic density anisotropies, we rely on cosmological dark matter (DM) only simulations, run with *Gadget-4* (Springel 2005; Springel et al. 2021) for the LEGACY project (Merlot et al. 2022).

L_{box} [Mpc/h]	1600	703.125	100	100
N_{eff}	2048^3	4096^3	2048^3	256^3
M_{res} [M_{\odot}]	5.43×10^{10}	6.78×10^9	1.32×10^7	6.78×10^9

Table 1. Simulations’ properties: L_{box} - comoving box length in Mpc/h, N_{eff} - effective particle number, M_{res} - mass resolution in M_{\odot} .

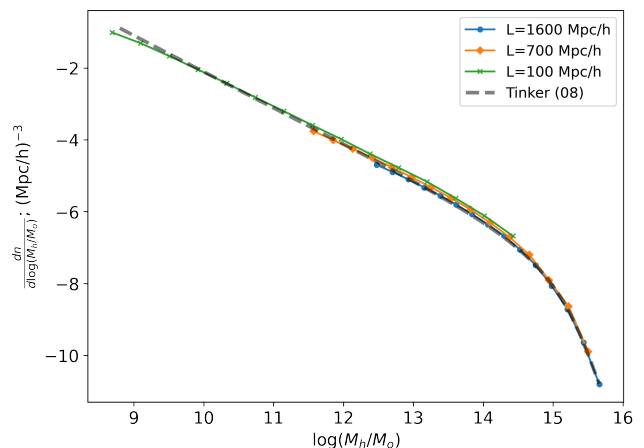


Figure 1. DM halo mass function for three of the large particle number LEGACY boxes that are used in the main analysis of this work. (Green solid) $L = 100$ Mpc/h, (Orange solid) $L \approx 700$ Mpc/h zoom-in simulation, and the $L = 1600$ Mpc/h box (Blue solid). Their mass functions are shown in the same order from left to right (as expected, only the largest box can form the more massive haloes). The grey dashed line provides the fit based on Tinker et al. (2008).

The latter is composed by two primary volumes of 1600 Mpc/h and 100 Mpc/h box sizes run down to $z = 0$ with 2048^3 resolution elements, as well as a set of zoom-in simulations on the larger box, with size 83 Mpc/h, and an effective resolution of 32768^3 (1700^3). The parameter h is defined as $h = H_0/100$. The latter have been designed to sample regions with density -2 , -1 , 0 , $+1$, and $+2 \sigma$ of the mean density of the Universe, as well as extremely high (cluster) and very low (void) density regions and are therefore ideal to study different environmental effects. We use ROCKSTAR (Behroozi et al. 2013a) to construct halo catalogues for each snapshot.

For our analysis, we use the data from four different boxes, at redshift $z = 0$, with box size of: $L_{\text{box}} = 1600, 703.125, 100$ Mpc/h. The details are shown in Table 1.

All simulations have an accompanying halo catalogue. The halo mass function for the large particle number runs is shown in Figure 1. The mass functions are consistent with the fit proposed in Tinker et al. (2008).

The cosmological parameters of the simulations, are taken from WMAP9 (Hinshaw et al. 2013), with $(\Omega_m, \Omega_\Lambda, \Omega_k, H_0) = (0.285, 0.715, 0, 69.5 \text{ km/s/Mpc})$.

2.1.1 Stellar-to-Halo mass connection

Since the simulations only follow DM, it is necessary to assign galaxy masses to individual haloes via models. Here we follow the standard parameterisation from (Yang et al. 2003; Moster et al. 2010), which relates halo mass to stellar mass of galaxies being

$\log M_{A,0}$	A_0	γ_0	β_0
11.77	0.0465	0.702	1

Table 2. Best fit values for eq. (1) from Girelli et al. (2020).

hosted by the halo, with the fit from Girelli et al. (2020):

$$\frac{M_*}{M_h}(z) = 2A(z) \left[(M_h/M_A(z))^{-\beta(z)} + (M_h/M_A(z))^{\gamma(z)} \right]^{-1}, \quad (1)$$

where the different parameters are given by (for $z = 0$, which is our redshift of interest):

- $\log M_A(z) = \log M_A(z = 0)$
- $A(z) = A_0$
- $\gamma(z) = \gamma_0$
- $\beta(z) = \beta_0$.

The fit⁴ in Girelli et al. (2020) is based on the subhalo abundance matching technique, where there is a one-to-one connection between halo (sub)structures and galaxies (see Neistein et al. 2011, for an investigation of this assumption).

The best-fit values from Girelli et al. (2020) are given in Table 2. In our simulations we assume the equivalent mapping of our haloes to galaxies and we use the two terms interchangeably from now on. Note that we ignore any scatter in the above relation, since for the level of complexity of this work, we are mainly interested in the general trend of galaxies’ masses. Masses, as well as the other physical weights, are not used for the majority of the analyses, except from section 3.2.2.

Finally we use ML to assign each galaxy an *absolute magnitude* in band B (M_B) and *star formation rate* (SFR) in M_\odot/yr . We choose these properties for consistency with Gray et al. (2020), and because the B-band acts as a proxy for SFR (Singer et al. 2016; Ducoin et al. 2020). A model is trained using the IllustrisTNG300 cosmological run (Springel et al. 2018; Marinacci et al. 2018; Naiman et al. 2018; Nelson et al. 2018; Pillepich et al. 2018) to predict these properties by taking subhalo spin, maximum rotational velocity, velocity dispersion and DM halo mass as input features. A complete description of this method can be found in (McGibbon & Khochfar 2022; Natarajan et al. 2023).

In summary, for each galaxy we have the following properties: 1) Their 3D coordinates, 2) their stellar mass, 3) their absolute magnitudes in the B band, and 4) their star formation rate.

2.2 Cosmological inference

In our analysis, we use halo catalogues from the different simulation boxes and estimate the effects of galaxy clustering and survey completeness on the determination of H_0 . Our general methodology tries to mimic as closely as possible the observational studies and consists of the following steps:

- *Step 1:* We place an observer at the centre of the box. We limit the maximum distance range to a sphere of $L_{\text{box}}/2$, which corresponds to about 1200, 506, and 72 Mpc radii, for the different boxes⁵.

⁴ The above fit is qualitatively very similar to other fits in the literature, (e.g. Moster et al. 2013; Behroozi et al. 2013b). We have confirmed that the specific selection is not influencing our results.

⁵ Note that here we include h in the calculation. As a reminder, the original box sizes were reported in units of Mpc/h.

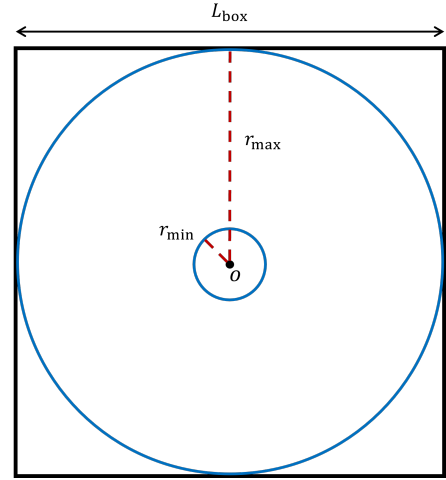


Figure 2. For each simulation we define an “observable spherical cell” in 3D. A 2D plane projection is shown here, with $[r_{\text{min}} = 10 \text{ Mpc}, r_{\text{max}} = L_{\text{box}}/2]$, as described in the main text.

We also define a minimum distance threshold of 10 Mpc. This means that for each case we only consider the galaxies that are within a spherical cell with range $[r_{\text{min}} = 10 \text{ Mpc}, r_{\text{max}} = L_{\text{box}}/2]$ In redshifts, the largest range covered is $z \in [0.005, 0.23]$, assuming the simulation cosmology (see also Figure 2).

- *Step 2:* We choose randomly a halo from the simulation catalogue: this is our ‘true’ GW source, with coordinates $(d^{\text{src}}, \theta^{\text{src}}, \phi^{\text{src}})$.

- *Step 3:* To avoid centering artificially our observational region at the ‘true’ source, we perturb the centre of our localisation cone. To find the new position, we construct a 2D Gaussian distribution centered at the ‘true’ source for the angular perturbation and a 1D Gaussian for the distance one, and draw a new position $(d^{\text{gw}}, \theta^c, \phi^c)$, c for ‘cone centre’. The latter will be the central point, around which we construct our localisation cone. The widths of this Gaussian distribution and the final cone depend on the observational errors we choose. These correspond to the distance uncertainty σ_{d_L} and the sky localisation errors σ_θ^2 of our detections. Section 2.3 provides the details of this procedure.

- *Step 4:* For all the haloes inside the cone, we find their distance to the observer. We also calculate the haloes’ projected angles on the sky as seen by the observer (see also Figure 7).

- *Step 5:* For all the haloes inside the cone, we calculate $H_{0,i}$, using their distance information, corresponding to the EM d_L , and the GWs distance d^{gw} (see section 2.5).

- *Step 6:* Finally, depending on the method (see section 2.6), we calculate the individual H_0 posterior for the cone.

- *Step 7:* For multiple events (cones), we repeat the procedure above and compute the final H_0 posterior distribution, by combining observations. The maximum number of GW events N_{gw} is specified for each case, with a fiducial number $N_{\text{gw,max}} = 100$, consistent with previous studies and the order of magnitude of the observed BBH mergers $N_{\text{BBH}} \sim 70$ from the first three observing runs (Abbott et al. 2019, 2021a, 2024, 2023a), and $N_{\text{BBH}} = 120$ from GWTC-4.0 (The LIGO Scientific Collaboration et al. 2025a).

We will describe some of these steps in more detail in the following sections. For a graphical summary, see Figure 3.

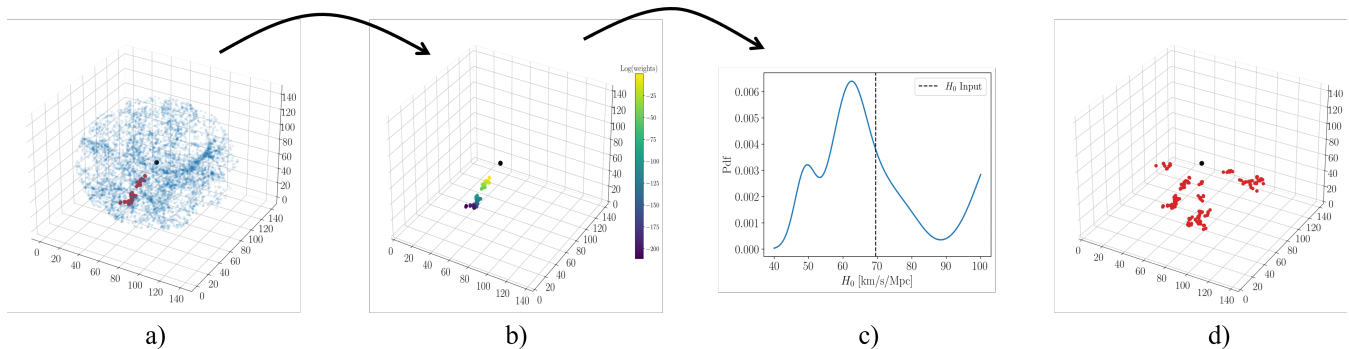


Figure 3. *Graphical summary of our analysis:* a) We cut an “observational sphere” from the test simulation box. A GW event is modeled as a 3D cone (red dots); b) the observer (black dot) is put at the centre of the “observational” sphere and the galaxies in the cone are assigned weights (geometrical or physical); c) each event produces an H_0 posterior; d) this procedure is repeated for multiple events and their H_0 posterior pdfs are combined. The $L_{\text{box}} = 100$ Mpc/h box, with fewer galaxies, has been chosen for visualisation purposes.

2.3 Error priors and choosing the GW source

To select our GW sources and construct our conical regions (section 2.4), we mimic the observational situation of real GW events (Soares-Santos et al. 2019). More specifically, we follow a procedure similar to Muttoni et al. (2022), who studied the multiband detection of massive BHs ($M_{\bullet} > 120M_{\odot}$) by a combination of future generation, ground and space based detectors, LISA (Amaro-Seoane et al. 2017) and Einstein Telescope (Maggiore et al. 2020; Branchesi et al. 2023).

Muttoni et al. (2022) used a Fisher matrix approach to estimate observational errors and to position their GWs sources. In our case, since we want to investigate the effects of different cone openings and sizes, we use a simplified, custom prescription to insert observational errors, described in more detail below and in section 2.4, but we position our GW sources in a similar way.

More specifically, there are two errors that are relevant in our case:

- A distance error σ_{d_L} , that corresponds to the error in the luminosity distance of the GW source. Here we model this error as a linear function of luminosity distance, i.e., $\sigma_{d_L} = A \cdot d^{\text{GW}}$, where A is a fixed proportion constant that we select in each simulated analysis.
- An angle error σ_{θ}^2 (or $\Delta\Omega$ below), that corresponds to the uncertainty of the sky localisation area (in units of squared degrees).

Usually, the errors quoted correspond to the 90% confidence interval⁶.

Based on these errors we build a theoretical 3D Gaussian distribution around the GW source, given by the product $\mathcal{N}(d^{\text{src}}, \tilde{\sigma}_{d_L})$ for the luminosity distance uncertainty and $\mathcal{N}(\theta^{\text{src}}, \tilde{\sigma}_{\theta})$ for the uncertainty in the two angles respectively. We consider the three errors as independent, and use them to draw the centres of our cones, by sampling them from these distributions. In other words, the original GW source and the centre of the cones, which act as the GW events’ 3D localisation, are in general, different.

In specific cases, described in section 2.4, the GW source needs to be discarded and a new random galaxy is to be selected. Then we repeat the procedure above, till all the criteria are satisfied.

We find that this procedure is robust and avoids introducing a

clear bias in our final results. Also, it is similar to observed signals, where the true source is not necessarily located exactly at the centre of the sky localisation region. In the *physics implementation*, we introduce some extra weights w_i before the selection of the GW source (section 2.6.2). Examples of the above procedure are shown in Figure 4.

These two errors ($A, \Delta\Omega$) are selected at the start of each simulated analysis, and are kept fixed for all events of the specific run. Below we study the impact of different error choices at the inference of H_0 (section 3.2.4), and we choose our ‘default’ values as $(A, \Delta\Omega) = (0.1, 60)$.

2.4 Cone construction

Based on the error selection (section 2.3), we can construct our cones. Their geometry is fixed as following: The height of the cone depends on the distance error σ_{d_L} and the H_0 prior range. More specifically, the limits of the cone would depend on how we model our distance likelihood (section 2.6.3). The default setting is a skewed Gaussian on the luminosity distance, following (Gair et al. 2022),

$$\begin{aligned} \mathcal{L}(d^{\text{GW}}|d_L(z, H_0)) &= \\ &= \frac{1}{\sqrt{2\pi}\tilde{\sigma}_{d_L}} \exp\left(-\frac{1}{2}\left[\frac{d^{\text{GW}} - d_L(z, H_0)}{\tilde{\sigma}_{d_L}}\right]^2\right), \end{aligned} \quad (2)$$

where d^{GW} is the distance of the ‘observed’ GWs event (centre of the cone) and the dependence of the error in the denominator on d_L , i.e. $\tilde{\sigma} \sim A \cdot d_L$ breaks the symmetry of the Gaussian, allowing a bigger ‘tail’ on larger distances.

Using this distribution, we calculate the extent of the cone. We use the cumulative distribution function of the distance likelihood, to find the distance range that corresponds to the 90% probability of the sky localisation:

$$p = \frac{1}{2} \left[1 + \text{erf}\left(\frac{d_L - d^{\text{GW}}}{\tilde{\sigma}\sqrt{2}}\right) \right]. \quad (3)$$

Solving for d , for the cases of $p = 5\%$ and $p = 95\%$, we find the minimum and maximum distances along the line of sight, d_L^5 and d_L^{95} respectively. Note that these limits would vary for a different underlying cosmology, so we take into account the H_0 prior range considered in this work. This will lead to a more extensive range of

⁶ This means that the standard deviation is $\tilde{\sigma} = \sigma/1.645$. The tilde sign (\sim) will be used to make this distinction clear, where needed.

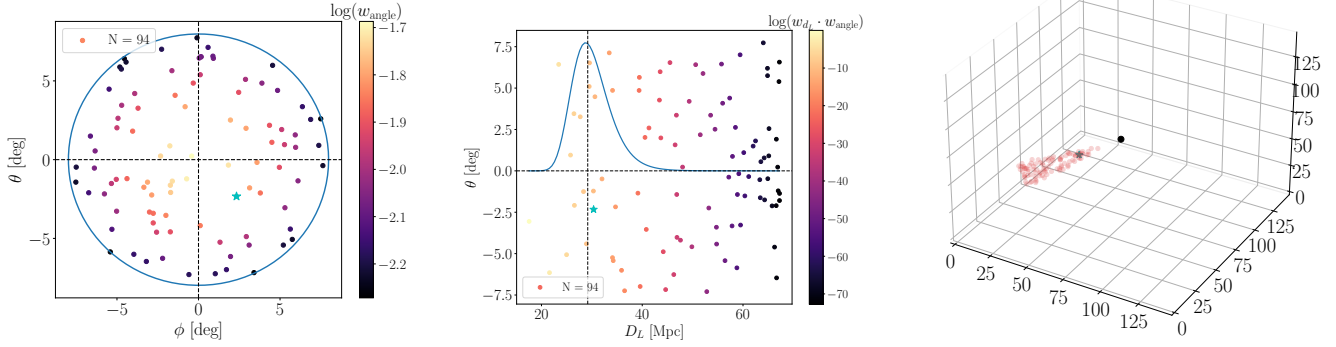


Figure 4. *Example of cone construction and of geometric weights:* We show one example of cone construction and the weights assigned to each galaxy inside the cone. The black, dashed lines show the coordinates of the cone centre, the cyan star shows the position of the true GWs source, while the other dots show the galaxies that belong to this cone. *Left:* We show the angular position of the galaxies (ϕ , θ), together with the geometric weights they are assigned with respect their position to the cone centre. *Centre:* Same cone, but from the side, with the x-axis, showing the luminosity distance of the galaxies. The weights here correspond to the combination of angular and distance weights $w = w_\theta \cdot w_L$ (see section 2.6.2). We also plot the distance likelihood, eq. (2) - blue, solid line. Note that the maximum distance of a galaxy inside the cone is bigger than the 95% range of the likelihood, and this is due to our consideration of the H_0 prior (recall section 2.4), i.e. for larger H_0 distances with the same redshift would be smaller, and as a result will be within the limits of our cone. *Right:* 3D configuration of the cone. The black dot corresponds to the centre of the box, i.e. the observer. The $L_{\text{box}} = 100$ Mpc/h box, with fewer galaxies, has been chosen for visualisation purposes.

distances [d_{\min} , d_{\max}]:

$$d_{\max} = d_L^{95} \times H_0^{\text{prior max}} / H_0^{\text{sim}} \quad (4)$$

$$d_{\min} = d_L^5 \times H_0^{\text{prior min}} / H_0^{\text{sim}}. \quad (5)$$

The details of this scaling are described in section 2.5 and in eq. (9). The above constrain the line-of-sight extent of the cone. Using this distance range we perform the first galaxy cut, i.e. we keep only galaxies with distances compatible with [d_{\min} , d_{\max}]. Additionally, we need to consider its angular opening. Although the sky localisation area is rarely a circle, we idealise it as such with our cone structure⁷. From the sky localisation area error $\Delta\Omega = \sigma_\theta^2$, we calculate the opening angle as $\theta = \sqrt{\sigma_\theta^2/\pi}$. The geometry can be seen in Figure 5. We calculate the radius of the cone for all distances as:

$$D_r(d_p) = d_p \tan \theta, \quad (6)$$

where d_p is the projected line-of-sight distance between a halo in the cone and the observer. Implementing this second constraint, we keep only the galaxies that lie within the cone.

Finally, when constructing the cones, we take into account some additional restrictions: since our observational sphere has a specific maximum limit (Figure 2), periodic boundary conditions should be imposed, or we need to constrain the regions where the cones can be constructed to avoid “overflowing” outside the box. We follow the latter option, i.e., we avoid placing our cones’ centres close to the boundaries. We note that this procedure could produce an “edge of the sphere” effect, where a hard-cut off on the presence of galaxies biases the H_0 inference. However, in our case we

avoid this problem by restricting the cone positions so they do not intersect the boundary of the box. This is mildly inconsistent, but can be considered as assuming that the statistical distribution of galaxies away from the boundaries of the box are representative of the distribution across the whole sky, which is a valid assumption for the volumes we use.

More specifically, we implement the following procedure:

- We choose a spherical geometry roughly consistent with the “horizon distance” of current, ground-based GW detectors.
- We impose a maximum distance of allowed galaxies’ positions $d_L^{\max} = L_{\text{box}}/2$, to avoid ‘overflowing’ outside the box, both for data generation and the H_0 inference.
- We impose a minimum distance of allowed galaxies’ positions $d_L^{\min} = 10$ Mpc, to avoid the observer being close to the cone, both for data generation and the H_0 inference.
- If a cone is created, such that a galaxy inside has a distance with $d_L > d_L^{\max}$ or $d_L < d_L^{\min}$, the cone is drawn again by selecting a new GWs source and centre - refer to section 2.3.

This procedure creates cones (events) which lie within our “observable spherical cell” (Figure 2).

2.5 H_0 calculation

The standard method to calculate the Hubble parameter at low redshifts ($z \ll 1$) is to use the approximation (Weinberg 2008):

$$H_0 = \frac{cz}{d_L}. \quad (7)$$

This relation is cosmology independent, but using it at higher redshifts can lead to a serious bias - towards lower values - in the measurement of H_0 , so extra care is needed (Davis & Scrimgeour 2014). In practice, for higher redshifts we cannot avoid the cosmological dependence (Davis & Scrimgeour 2014), so we have to either keep extra redshift terms in the luminosity distance expansion

⁷ An asymmetry in the sky localisation, as in most real events, will introduce two opposite effects. On the one hand, it could improve determination of H_0 , since some galaxies will be disfavoured more clearly, based on their position. On the other hand, it usually includes a higher number of galaxies, flattening the H_0 posterior. In the final analysis, the two approaches should be statistically equivalent, as long as the regions are big enough to include the large-scale structure effects of interest. We comment further on that in Figure 6 and in section 3.

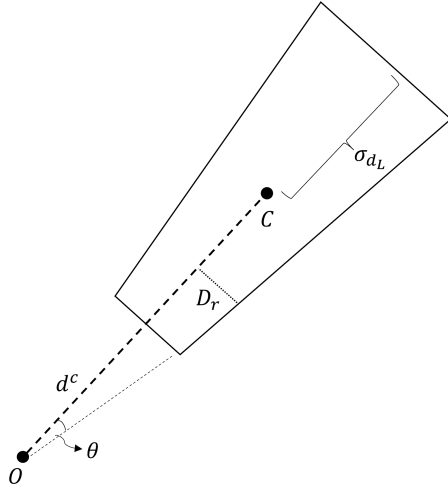


Figure 5. The most important distances in our cone construction. See discussion in section 2.4 for details.

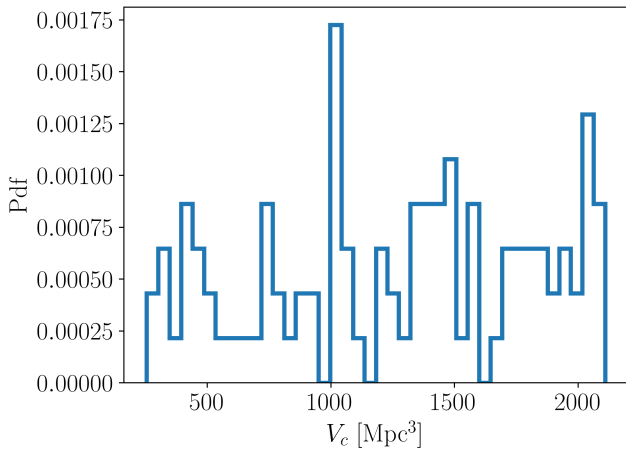


Figure 6. As discussed in section 2.4, the shape of our sky region should not, statistically speaking, affect the results, as long as our regions are large enough to contain large-scale structure information. We plot here a histogram of the volume of each cone, in a run with $N = 100$ events in the $L_{\text{box}} = 100$ Mpc/h. The size of the cones, even in that case, is large enough, such that no bias is expected from the shape of our cuts.

or fit the standard luminosity distance for a flat, Λ CDM universe:

$$d_L(z) = (1+z) \frac{c}{H_0} \int_{(1+z)^{-1}}^1 \frac{da}{\sqrt{\Omega_m a + (1-\Omega_m)a^4}} = \frac{K(z)}{H_0}, \quad (8)$$

where we have neglected the contribution of cosmic radiation and have introduced the scale-factor a , with $a_0 = 1$. The distance is obtained from the GW observation $d_L = d^{\text{gw}}$ and the redshift from the photometric or spectroscopic information of the galaxies in the catalogue. As a result, one can marginalise over luminosity distance and redshift information, to infer the different cosmological parameters. This general procedure does not use any approximation for the expression of the luminosity distance and would be valid for future GW observations, which are expected to reach $z > 1$ (Chen et al. 2024). For this work, all cosmological parameters are fixed to the values of the simulations, and we only infer H_0 .

Then, we have for each galaxy in the sky localisation:

$$H_0^g = H_0^{\text{sim}} \frac{d_L^g}{d^{\text{gw}}}. \quad (9)$$

H_0^g corresponds to the inferred Hubble parameter for galaxy g , H_0^{sim} to the injected one, i.e., the one used in our simulation, d^{gw} the distance inferred from the GW observation, i.e., the centre of the cone in our case and d_L^g the distance of a galaxy within the conical region. This procedure gives us, for each cone, N values of H_0^g , one for each galaxy d_L^g . Note that we first select the cone centre d^{gw} , which is then kept fixed for the specific cone.

To understand the validity of this relation, we start from equation (8). Assuming the redshift of a galaxy is z^g , this will lead for a given H_0 to a distance $d_L^g = K(z^g)/H_0$. If we assume that this galaxy is the source of the GW event, then $d_L^g = d^{\text{gw}} \Rightarrow H_0^g = K(z^g)/d^{\text{gw}}$.

Since the simulations provide the coordinates of the galaxies (instead of redshifts), and through them one can easily obtain distance information with respect to an observer, we modify this relation to

$$H_0^g = \frac{K[z^g(d^g, H_0^{\text{sim}})]}{d^{\text{gw}}}. \quad (10)$$

We note that $K(z^g) = d_L^g \cdot H_0^{\text{sim}}$, i.e. we use the simulation cosmology H_0^{sim} to connect a given distance with a redshift, and hence we can write

$$H_0^g = H_0^{\text{sim}} \frac{d_L^g}{d^{\text{gw}}}. \quad (11)$$

The distances are calculated directly from the coordinate information given by the simulation⁸.

The injected value of H_0^{sim} , as well as the other cosmological parameters, are taken from WMAP9 (Hinshaw et al. 2013), in order to be consistent with our cosmological simulations.

The preceding arguments indicate that the main contribution to the H_0 estimate will come from the relative position of each galaxy in the region compared to the estimated location of the GW source. This formulation makes clear the positive effect of clustering to the final statistics. When clustering is present, there will be a higher probability that the true source is grouped together with other galaxies in the region, and as a result, share similar distances.

Finally, we note that this procedure to calculate H_0 is used directly in section 2.6.1, where we ‘stack’ the H_0 values of all the galaxies in the sky localisation areas of the events. In section 2.6.3, where we develop a Bayesian analysis to infer H_0 we use this procedure to update the distances of the galaxies, but not to calculate H_0 directly.

2.6 H_0 posteriors

To calculate the posterior on H_0 we follow two different methods, of increasing complexity and similarity to observational techniques. We analyse them in turn.

2.6.1 H_0 stacking

This case extends the work of MacLeod & Hogan (2008). In their work, they consider:

⁸ For the respective redshift ranges, we assume that comoving and physical distances are the same. However, this will not affect the final conclusions of our work, since we are interested in distance ratios.

- Boxes, as the localisation volume, which avoid realistic geometry biases.
- Galaxies with equal weights, i.e., they are not weighted based on their true position in the box.
- Very precise distance determination, which would be more relevant for LISA (Amaro-Seoane et al. 2017).
- GW events with equal weights, i.e., irrespective of the number of galaxies in the box/sky uncertainty.

In our implementation of this method, we aim to improve on these assumptions, making the following changes:

- We implement a more realistic sky localisation, both in terms of capabilities of current ground-based GWs detectors, but more importantly in terms of the sky volume, i.e., using skewed cones, instead of square boxes.
- We include geometric and physical weights for each galaxy (section 2.6.2).
- We simulate a uniform catalogue, to estimate the importance of clustering, by comparing to a realistic catalogue from cosmological simulations.
- We take into account the different quality of each GW event (section 2.6.2).

For the simpler case of ‘ H_0 stacking’, or ‘histogram analysis’, we follow equation (9).

This means that for each cone we have N_c values of H_0^g , where N_c is the number of galaxies in the cone. When considering the final H_0 histogram, we stack together all these H_0^g values from multiple cones/events.

Finally, we note a couple of things:

(i) Firstly, the centre of the cone does not correspond to the coordinates of any specific galaxy, since the cone centre is perturbed away from the true host galaxy by the observational error - sections 2.3 and 2.4.

This means that we do not induce an artificial peak towards the input value H_0^{sim} , and more clearly demonstrates the power of the method, and in particular clustering, since we recover H_0^{sim} even without any knowledge of the ‘true’ host galaxy of the source.

(ii) Secondly, unless a correction is made, this ‘stacking’ method will have a clear bias to higher values of the Hubble-Lemaître parameter, because of geometric effects, i.e., more galaxies are in the far side of the cones. To make this clearer we return to equation (9). The cone centre distance d^{gw} , is the geometric centre of the cone. However, due to the cone geometry, with consecutive rings covering more volume at larger distances, this leads to an increased number of galaxies with $d_L^g > d^{\text{gw}}$, and from equation (9), $H_0^g > H_0^{\text{sim}}$.

A consistent resolution to these “volume” effects is described in section 2.6.3, where the full likelihood is calculated. To address these in the simplified “stacking” method, we introduce the GWs measurement errors as weights and build a “weighted histogram”, where each galaxy’s contribution is weighted by its position in the cone, using the weights from section 2.6.2.

The results of this method are discussed in section 3.1.

2.6.2 Geometric and Physical Weights

For each galaxy we have information about its position inside the cone, both in terms of distance from the observer, but also its sky coordinates. So, we have a luminosity distance between the galaxy and observer d_L^g and a pair of angles (ϕ, θ) depending on sky position. Hence, we can use the observational errors to assign geometric

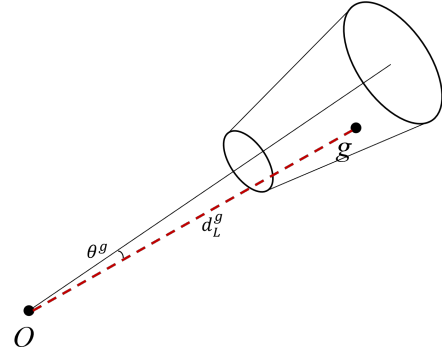


Figure 7. To calculate the geometric weights for each galaxy g , we use its angle θ^g with respect to the centre of our observational cone, and its luminosity distance d_L^g . See discussion in section 2.6.2 for details.

weights to the galaxies. In the full analysis - section 2.6.3 - these weights are part of the likelihood construction: a priori each galaxy is considered equally likely to be the host of the GW event. However, in the presence of GW data, specific sky locations and distances are disfavoured as hosts of the true source by the GW likelihood. For the ‘ H_0 stacking’ method - section 2.6.1 - these are included as additional weights when constructing the histograms. The weighting is based on the galaxies’ coordinates versus the coordinates of the ‘observed’ GW, at the centre of the cone. For the luminosity distance:

$$w_L \sim \exp \left[-\frac{1}{2} \left(\frac{d_L^g - d^{\text{gw}}}{\tilde{\sigma}_{d_L}} \right)^2 \right], \quad (12)$$

where we recall that $\tilde{\sigma}_{d_L} = \sigma_{d_L}/1.645$, since σ_{d_L} corresponds to the 90% confidence interval. For the angles, we exploit the symmetry of the cones and define their angular position with respect to the line-of-sight between the observer and the cone centre (Figure 7).

The weight is then given by:

$$w_\theta \sim \exp \left[-\frac{1}{2} \left(\frac{\theta^g - \theta^{\text{gw}}}{\tilde{\sigma}_\theta} \right)^2 \right]. \quad (13)$$

Apart from the above geometric weights, we also include, in some runs, weights based on the physical properties of the galaxies - magnitude, star formation rate or stellar mass - as a simple multiplicative factor. For example, for masses, we calculate a weight for each galaxy $w_M^g = M^g / \sum_i M^i$. The weights can be used to penalise the contribution of individual galaxies to the final H_0 posterior, the selection of hosts for GW sources or both. To avoid any statistical bias due to low number of galaxies inside each cone, we calculate the physical weights based on the initial catalogue, with all the galaxies present, not including only the cone galaxies for each event.

2.6.3 Bayesian analysis

We now develop a Bayesian analysis to calculate the posteriors of H_0 . We follow the approach in Del Pozzo (2012); Chen et al. (2018); Muttoni et al. (2022); Gair et al. (2022). From Bayes’ theorem, we have:

$$P(H_0|D) = \frac{P(D|H_0)P(H_0)}{\mathcal{Z}}, \quad (14)$$

where the different terms are:

- $P(H_0)$: Prior degree of belief on the H_0 value. We assume a flat distribution with $H_0 \in [40, 100]$ km/s/Mpc. Recall our input value from the simulations is in the middle of this range, with $H_0^{\text{sim}} = 69.5$ km/s/Mpc.

- $P(D|H_0)$: Likelihood of the data, given an H_0 value and a model. We are going to assume (skewed) Gaussian distributions for the modelling (see below).

Data here are the observed distances and positions of the GW sources. The cosmological parameters, other than the Hubble-Lemaître parameter, are fixed as described in section 2.1.

- \mathcal{Z} : The evidence. We are going to ignore this, since we are going to normalise our posterior at the end.

For each cone, we calculate a likelihood $\mathcal{L}(D^{\text{gw}}|H_0)$. Since each cone corresponds to a single, independent event, the full likelihood for N_c events is:

$$P(D|H_0) = \prod_c^{N_c} \mathcal{L}_c(D^{\text{gw}}|H_0). \quad (15)$$

Each cone/event includes the contributions of all the galaxies in the sky localisation volume, which yields for the single likelihood:

$$\mathcal{L}_c(D^{\text{gw}}|H_0) \propto \sum_g^N \mathcal{L}_g(D_c^{\text{gw}}|H_0), \quad (16)$$

where N is the number of galaxies in the cone. This likelihood includes a number of terms, which we analyse in order below. For now, we ignore any physical weights, i.e. we assume that the GW host can be any of the galaxies in the cone. However, the position of each galaxy in the cone (d_L, θ) enters the GW observation likelihood:

$$\mathcal{L}_{\text{gw}}(d_L^c, \theta^c | d_L, \theta) \sim p(d_L^c | d_L) p(\theta^c | \theta), \quad (17)$$

where we have assumed that the two contributions are independent. More specifically, we model them as (skewed) Gaussians:

- $p(\theta^c | \theta)$: how far in the sky is the position θ in the cone compared to the cone centre.

$$p(\theta^c | \theta) \sim \exp \left[-\frac{1}{2} \left(\frac{\theta - \theta^c}{\tilde{\sigma}_\theta} \right)^2 \right]. \quad (18)$$

In the following, we assume that we can pinpoint exactly the sky location of each galaxy, i.e. $p(\theta | \theta^g) = \delta(\theta - \theta^g)$, where δ is the Dirac δ -function.

- $p(d_L^c | d_L)$: the likelihood of each luminosity distance compared to our GWs information. We use the form adopted in Gair et al. (2022):

$$p(d_L^c | d_L) \sim \frac{1}{\tilde{\sigma}_{d_L} \sqrt{2\pi}} e^{-\frac{1}{2} \left(\frac{d_L - d_L^c}{\tilde{\sigma}_{d_L}} \right)^2}, \quad (19)$$

where $\tilde{\sigma}_{d_L} \sim A d_L(z, H_0)$, with A the factor discussed in section 2.3.

The distance information of the galaxies comes through their redshifts and a set of cosmological parameters (in our case H_0), through eq. (8), $d_L = K(z)/H_0$. Hence, for a given cosmological model only one of d_L, z is independent:

- $p(d_L | z, H_0)$: how we infer our distances given the redshift and cosmological parameters:

$$p(d_L | z, H_0) = \delta(d_L - d_L(z, H_0)). \quad (20)$$

The galaxies' redshifts come from EM observations, with their own uncertainties, which introduces a redshift probability $p(z | z^g)$.

- $p(z | z^g)$: how good is our knowledge of the galaxies' redshifts. For this we assume perfect knowledge of the galaxies' redshifts, i.e. $\delta(z - z^g)$. In the case of uncertain redshifts, we tested a Gaussian model:

$$p(z | z^g) \sim \exp \left[-\frac{1}{2} \left(\frac{z^g - z}{\sigma_z} \right)^2 \right], \quad (21)$$

where σ_z is the net error in the redshift determination. We find that the main results of our work are unaffected, and since our main emphasis is on the effects of clustering and incompleteness, in the following we use precise galaxy redshifts. A detailed analysis of redshift effects on H_0 inference with “dark sirens” can be found in Turcki et al. (2023); Cross-Parkin et al. (2025).

Putting everything together, and marginalising over the range of relevant distances, redshifts and angles, the single cone likelihood becomes:

$$\begin{aligned} \mathcal{L}_c(D^{\text{gw}}|H_0) &= \int dd_L dz d\theta p(d_L^c | d_L) p(\theta^c | \theta) \cdot \\ &\cdot p(d_L | z, H_0) p(z | z^g) p(\theta^c | \theta) \cdot \\ &\propto \sum_g^N p(d_L^c | d_L^g(H_0)) \mathcal{N}(\theta^c | \theta^g). \end{aligned} \quad (22)$$

We should note that all the z integrals above, range from z_{min} to z_{max} , constructed to cover the full cone constructed by $d^{\text{gw}} \pm \sigma_d$, transformed to redshifts taking additionally into account the H_0 prior range. In practice, this means that we consider galaxies in the distance range $[d_{\text{min}}, d_{\text{max}}]$, defined in section 2.4.

Extra weights w_g can be included for each galaxy, that depend on other physical characteristics, like mass, star formation rate, or B-mag, as described in section 2.1. Then we get:

$$\mathcal{L}_c(D^{\text{gw}}|H_0) \propto \sum_g^N p(d_L^c | d_L^g(H_0)) \mathcal{N}(\theta^c | \theta^g) w_g. \quad (23)$$

To create the final posterior distribution, we calculate the likelihood above throughout the prior range of H_0 .

Unless the *physics implementation* is selected, we set $w_g = 1$, otherwise we use normalised weights based on physical properties of the galaxies. For example, if we weight with the masses, we define $w_g = m_g / \sum m_g$, where the sum extends to all the galaxies in the catalogue.

Finally, it is important to take into account GW selection effects, i.e., the importance of each event based on how likely they are to be detected (Gray et al. 2020; Muttoni et al. 2022; Gair et al. 2022). For this reason, we divide the likelihood of each cone with

$$P_{\text{det}}(H_0) = \sum_g^N P_{\text{det}}(z_g, H_0), \quad (24)$$

where the detection probability $P_{\text{det}}(z_g, H_0)$ is given by

$$P_{\text{det}}(z, H_0) = \frac{1}{2} \left[1 + \text{erf} \left(\frac{d_L^{\text{thr}} - d_L(z, H_0)}{\sqrt{2} A d_L(z, H_0)} \right) \right], \quad (25)$$

where d_L^{thr} corresponds to the threshold distance where we can observe GW events. Since we only allow GW events, where their relevant cones are within our observational sphere, the maximum distance allowed is smaller than $L_{\text{box}}/2$ and depends on the observational errors we assume for each analysis. More specifically, it is calculated as

$$d_L^{\text{thr}} = L_{\text{box}}/2 \cdot H_0^{\text{min}}/H_0^{\text{sim}} \cdot \cos(\theta)/(1 + A), \quad (26)$$

with A the proportionality constant of the luminosity distance error, as described in section 2.3, while θ correspond to the opening angle of the cone radius, as shown in Figure 5. The latter corrects for the fact that the maximum distance from the observer in a cone, is not the line-of-sight direction, but the point that corresponds at the edge of the cone. The selection effects for each box are calculated once at the beginning of each run.

Finally, our likelihood for a single cone is updated to

$$\mathcal{L}_c(D^{\text{gw}}|H_0) \propto \frac{\sum_g^N p(d_L^c|d_L^g(H_0))\mathcal{N}(\theta^c|\theta^g)w_g}{P_{\text{det}}(H_0)}. \quad (27)$$

We now have all the tools in order to infer H_0 from dark sirens in simulations!

2.7 Investigating completeness

The power of the statistical method lies in our capability to cross-correlate the GW sky localisation volume with the galaxies in the region.

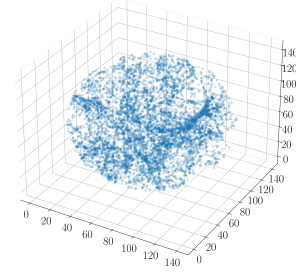
So far, we have assumed perfect knowledge of all the galaxies that reside inside our observational sphere. However, in realistic scenarios, not all galaxies inside the sky localisation volume are observable. This is due to observational limitations of the EM surveys which are likely to produce galaxy catalogues that are incomplete, i.e., with galaxies missing due to specific sensitivities in magnitude.

In these cases, the standard procedure, that we also follow here, is to complete the catalogue, based on the mean density of the Universe for the specific volume, by uniformly adding galaxies back. Note that this method is similar, but not the same as in [Chen et al. \(2018\)](#); [Gray et al. \(2020\)](#), where the contribution of the missing galaxies is calculated statistically. In our case, we add galaxies back in the catalogue and take their contributions into account as described in section 2.6. We note that for the added galaxies we have only geometrical information, and do not assign physical characteristics, i.e., in the analysis we only consider their positions in the sky. In future work ([Barbieri et al. 2025](#)), we are expanding this framework, in order to complete the galaxy catalogues exploiting prior clustering information, but also by assigning physical properties, like magnitudes.

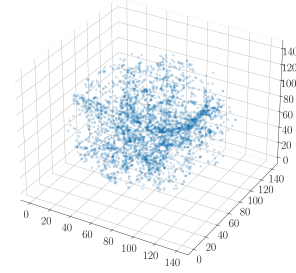
To investigate completeness effects, we include a ‘‘completeness fraction’’ f in our data generation. This selects a percentage of the original galaxies in our observational sphere that remain in the incomplete catalogue, based on specific physical thresholds. For this reason, we adopt a selection procedure that tries to mimic observational studies by removing galaxies based on magnitude:

A fraction of the least ‘‘bright’’ galaxies is removed, which replicates the magnitude limitations in a survey. Following [Gray et al. \(2020\)](#), these depend on the distance of the galaxies from our observer and, in our case, their absolute (B -band) magnitude. So the relevant magnitude formula becomes: $m = M_B + 5 \log_{10}(d_L/\text{Mpc})$, where we have neglected the constant factors, since we are only interested in a galaxy fraction, and not absolute numbers.

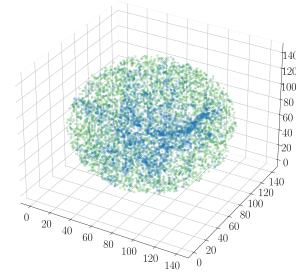
The selection cuts are performed taking into account the properties of the galaxies of the observable sphere. For a concrete example, refer to section 2.7.1. This leads to a completeness fraction estimated via $f = N^{\text{survived}}/N^{\text{all}}$. This is a ‘‘global’’ completeness level, hence note that there are expected to be significant variations in the completeness of individual cones. This is expected in a realistic scenario, since the magnitude cut introduces a distance scale, i.e., closer-by galaxies are most likely to be observed in all cases, hence closer-by GW events will have more complete cones. For our



(a) Initial Sphere



(b) Sphere after a 50% cut



(c) Uniformly Completed Sphere

Figure 8. Example procedure of creating an incomplete catalogue and then completing the missing galaxies, sampling from the uniform sphere. This example describes a 50% magnitude cut, i.e., throwing away half the galaxies, based on their magnitudes. The $L_{\text{box}} = 100$ Mpc/h box, with fewer galaxies, has been chosen for visualisation purposes.

analysis, we choose to retain the global percentage cut, which more closely resembles an observational scenario.

Unless stated otherwise, we investigate four incompleteness fractions f , that correspond to $f = 75\%$, 50% , 25% and 5% survey completeness.

2.7.1 How to complete the catalogue?

We complete the catalogues, exploiting a ‘sampling’ uniform box, i.e., put galaxies back that are uniformly distributed in comoving volume, as is the standard procedure in the literature ([Soares-Santos et al. 2019](#)). A method to complete the catalogues retaining clustering information is developed in the complementary work of [Barbieri et al. \(2025\)](#).

A better way to understand our method is with a specific example - see also Figure 8. Assume that we want to create a catalogue of $f = 50\%$ completeness and uniformly add galaxies back. We follow the steps below:

- (i) We start with the complete, clustered observable sphere.

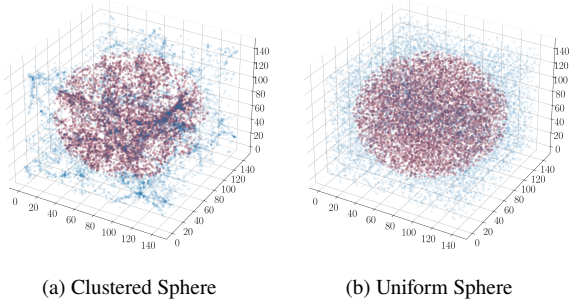


Figure 9. Construction of “observable spheres” in: (a) a clustered catalogue and (b) a uniform catalogue. The $L_{\text{box}} = 100$ Mpc/h box, with fewer galaxies, box has been chosen for visualisation purposes.

For the largest box, this corresponds to a sphere with radius $r = L_{\text{box}}/2 = 800$ Mpc/h.

(ii) We use the ‘magnitude cut’ method, to throw away 50% of the galaxies, i.e., we remove the 50% of galaxies with the highest apparent magnitude.

(iii) Now our catalogue is only 50% complete and we need to fill it again with galaxies to reach the same density of galaxies. The number of galaxies we need is estimated from a comparison to the initial clustered catalogue⁹: for the same radial bin in the original box, how many galaxies are missing compared to the 50% cut radial bin? This is N_{missing} per bin.

(iv) From a ‘uniform box’, see section 2.8, we cut again an ‘observable sphere’ of the same size as the initial one, $L_{\text{box}}/2$.

(v) From the uniform sphere, we draw randomly N_{missing} galaxies, without replacement (to avoid drawing the same galaxy coordinates more than once), from the distance bins where we have missing galaxies.

(vi) We combine the 50% clustered galaxies and the 50% uniform galaxies, to have a new “complete” catalogue, in our observable sphere.

(vii) This sphere is now the basis of our analysis for the H_0 posterior of the $f = 50\%$ case. It can be used as input to the analyses described in section 2.6.

2.8 Uniform box

In order to quantify the effects of clustering, we aim to compare with previous similar studies (Chen et al. 2018; Gray et al. 2020), but also perform our own baseline analysis for better consistency. For this reason, we create a simulation box with uniformly distributed galaxies to compare the consequences of clustering versus a randomly, uniformly populated catalogue. This dataset includes only information about the galaxy coordinates, without any physical properties.

The comparison box has the same number of galaxies as the clustered one. Since we only use an observable spherical region for the clustered case, we need to perform the same cut in the uniform box (Figure 9). Results will be presented for these two spheres: one with galaxy clustering and one with uniformly distributed galaxies. The procedure to calculate the H_0 posterior is the same as described in section 2.6.

⁹ We have checked that the original box used for comparison, either the clustered one or the uniform one, does not introduce any significant change on the results of completion.

2.9 Multiple realisations

Finally, to study the robustness of our results and estimate cosmic variance, we run multiple realisations of our analysis. This means that we repeat the analysis for the final H_0 posterior for a given number of cones (events) N_c , multiple times N_r . Each realisation draws different cones and repeats the catalogue completion, i.e., draws new random galaxies from the uniform, sampling catalogue.

To be more explicit, when we investigate the result of N_c cones, a single run will return an H_0 posterior, which could be described by a mean $\langle H_0 \rangle$ and error σ_{H_0} , for these N_c events¹⁰.

If we repeat the run N_r times, we have:

- $\langle H_0 \rangle_1^c, \langle H_0 \rangle_2^c, \dots, \langle H_0 \rangle_r^c, N_r \langle H_0 \rangle$ values.
- $\sigma_1^c, \sigma_2^c, \dots, \sigma_r^c, N_r \sigma_{H_0}$ values.

We then combine the results of the separate realisations as:

$$\bar{H}_0 = \frac{1}{N_r} \sum \langle H_0 \rangle_i^c \quad (28)$$

$$\bar{\sigma}_H = \frac{1}{N_r} \sum \sigma_i^c \quad (29)$$

$$\delta \bar{\sigma}_H = \sqrt{\frac{1}{N_r} \sum (\sigma_i^c - \bar{\sigma}_H)^2}. \quad (30)$$

These give respectively an average value of $\langle H_0 \rangle$, an average value of the posterior width over realisations, and the standard deviation of the posterior widths over realisations. We also cross-check our method by adding together the full posteriors of each realisation, which are used for the final results. We use $N_r = 15$ realisations, as the default. Recall that in all these cases, the initial, complete, clustered galaxy catalogue is the same, with each realisation having different cones’ positions. For the incomplete catalogues, apart from the new positions of the cones, for each realisation we construct a new $f\%$ catalogue, by drawing new galaxies in place of the ones that are missing.

3 RESULTS

We now investigate the H_0 inference, considering the main analysis methods of section 2.6. We also discuss the effects of incomplete catalogues and the consequences of the different geometrical or physical weights.

3.1 Histograms stacking

The simplest way to estimate the Hubble parameter is to stack the H_0 values from all the galaxies, from multiple cones. The results can be seen in Figures 10 and 11. For all the plots we use $N = 100$ events, while we compare resolution effects by using the $L_{\text{box}} = 100$ Mpc/h, small particle number box (Figure 10 (b)), and $L_{\text{box}} = 1600$ Mpc/h simulation (Figure 11).

In Figure 10 we investigate the importance of penalising the galaxies with geometric weights (recall section 2.6.2). The inclusion of weights is important to correct for the geometric effects of the cone. At the same time, it improves the convergence of the final

¹⁰ The final posterior, in most cases, is nicely approximated by a Gaussian since $N_c \gg 1$, so the mean and error give a good description of the final distribution. We checked that the results of combining the full posteriors are equivalent. In our analyses, we use the full posteriors.

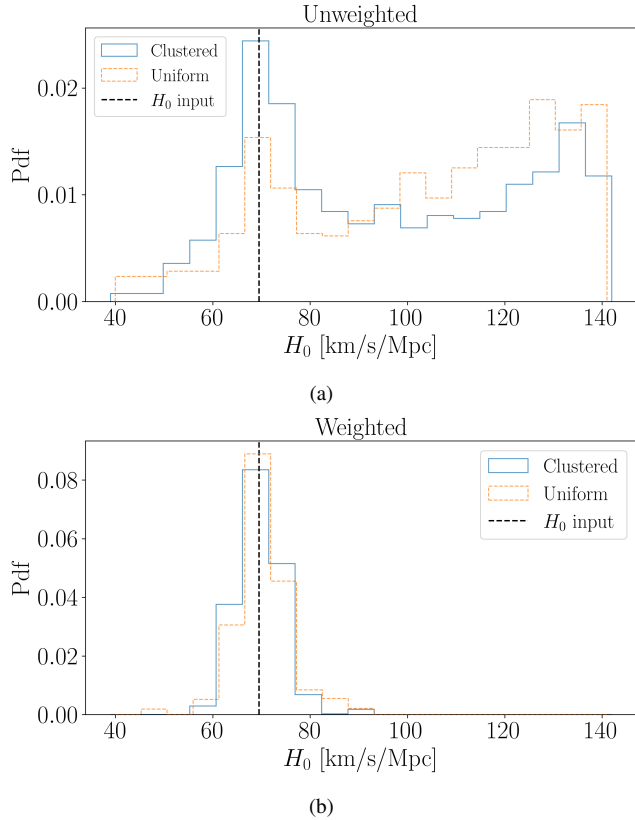


Figure 10. Stacking histograms for the Hubble parameter for a clustered (blue, solid) and a uniform (orange, dashed) catalogue. The top figure (a) does not involve any weighting and it is biased towards large values of H_0 , while the bottom figure (b) penalises galaxies based on their position with respect to the cone centre. This correction is needed when realistic detection geometries are used. We have used $N_c = 100$ events from the $L_{\text{box}} = 100$ Mpc/h box.

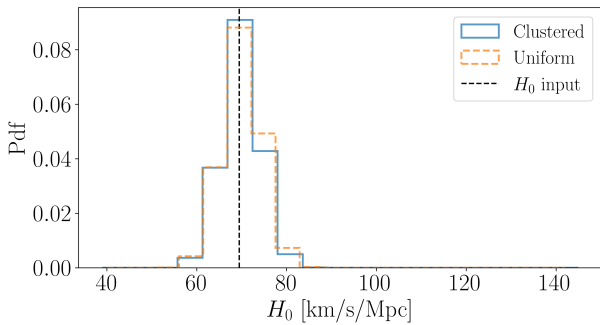


Figure 11. Stacking histograms for the Hubble parameter for a clustered (blue, solid) and a uniform (orange, dashed) catalogue. In both cases, we recover the input value. Both catalogues give equivalent results. We have used $N_c = 100$ events from the $L_{\text{box}} = 1600$ Mpc/h box.

histogram. In all Figures we plot the histogram of the stacked H_0 , where the solid line corresponds to the clustered case, while the dashed line to the uniform one.

The power of clustering is not clear in this basic approach, although in the unweighted case, the presence of clustering enhances the peak around the input value. The clustered distribution is similar to the uniform one, for both boxes. To quantify the difference, the calculation of the interquartile gap ($\sigma_q = q_{75} - q_{25}$),

gives $\sigma_q^{\text{clu}} \approx 11$ vs $\sigma_q^{\text{uni}} \approx 16$ for the small box, when comparing the clustered and uniform cases respectively. Similarly, $\sigma_q^{\text{clu}} \approx 11$ vs $\sigma_q^{\text{uni}} \approx 10$ for the large one. The small difference between the small and large cases, and clustered and uniform catalogues can be attributed to the analysis method: the events are not considered as independent, and the process of stacking all the H_0 values together leads to “smoothing” the final histogram, around the input H_0 value, which we recover successfully in all cases.

We should emphasize again, that in our analysis we ignore the contributions of the true GWs sources, since the cone centres are perturbed from the true source and are not required to reside on a galaxy.

This makes our results stronger, demonstrating that the knowledge of the true source is not necessary for accurate inference (see also (Bera et al. 2020)).

3.2 Bayesian analysis results

In this section, we investigate how the H_0 Pdfs are affected by the number of GWs observations (subsection 3.2.1), the presence of physical weights (subsection 3.2.2), catalogue completeness (subsection 3.2.3), observational errors (subsection 3.2.4), the inclusion of angular weights (subsection 3.2.5), box size (subsection 3.2.6), the method of completion (subsection 3.2.7), and the H_0 prior selection (subsection 3.2.8). Finally, we examine converge issues (subsection 3.2.9).

As a reminder, the default settings correspond to:

- *Box size:* $L_{\text{box}} = 1600$ Mpc/h simulation.
- *GWs events:* Number of events $N_c = 100$ and number of realisations $N_r = 15$.
- *Observational errors:* $(\Delta\Omega, 100 \cdot A) = (60, 10)$.
- *Weights:* Physical weights - None, Geometrical weights - distance and angle weights.
- *Pdfs Normalisation:* The normalisation is arbitrary, but consistent among the different analyses.

3.2.1 Convergence with number of events

In Figure 12, we explore the evolution of H_0 posteriors with increasing number of events. These runs use the large, $L_{\text{box}} = 1600$ Mpc/h box, where different numbers of events are chosen from the complete catalogue and averaged over $N_r = 15$ realisations. We confirm the anticipated behaviour: the posteriors become tighter with increasing number of events. Moreover, the scaling of the Pdfs follow the expected $1/\sqrt{N}$ scaling of the standard error of the mean. Finally, we note that when increasing the number of events, we are not adding cones to the previous ones, but doing a completely new H_0 inference run, with independent GWs events.

3.2.2 Effects of physical weights

Figure 13 investigates the importance of physical weights, specifically of masses, magnitudes (Mag B) and star formation rates (SFR). The latter are calculated for each halo using the ML techniques developed in (McGibbon & Khochfar 2022) and are assigned in the analysis as linear weights (section 2.6.2). We analyse four cases:

- Case 1:* We use physical weights in the GW selection procedure, e.g., for mass weights, more massive galaxies would be chosen preferentially as the sources of GW events. However, we ignore weights when estimating H_0 .

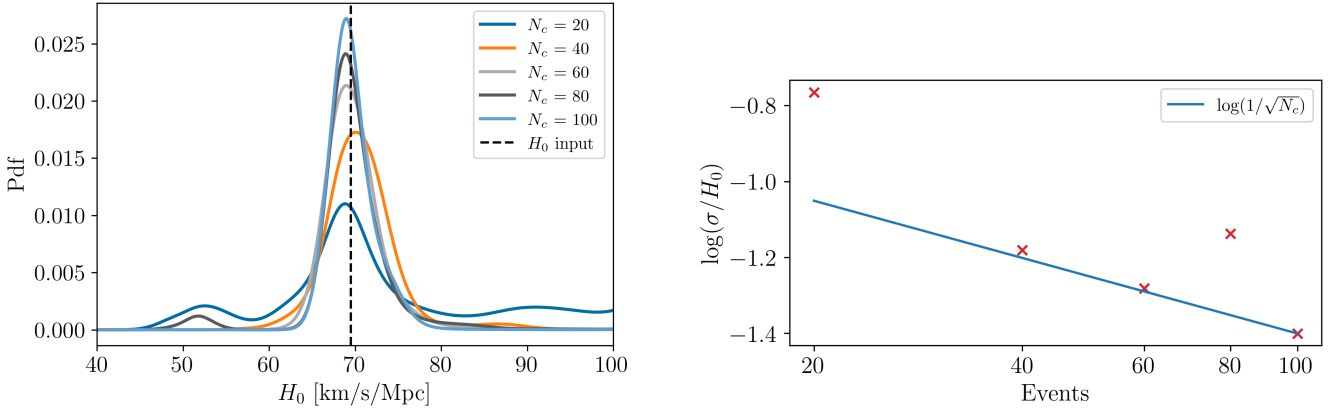


Figure 12. (Left): H_0 posteriors with increasing number of events (from $N_c = 20$ to $N_c = 100$ GWs events) and $N_r = 15$ realisations for each. As expected, more observations lead to tighter constraints. (Right) The mean standard deviation of the final posterior for all realisations for the specific number of events, compared to the input $H_0 = 69.5$ km/s/Mpc. We compare with the expected scaling of $1/\sqrt{N_c}$ (solid line) in log space, normalised to the most accurate posterior (of $N_c = 100$ events). Note that the presence of tails or bumps in the posteriors of $N_c = 20, 80$ lead, unsurprisingly, to deviations from the expected behaviour (since the standard deviation assumes a well-shaped Gaussian), which is nevertheless observed for all other cases. We have checked by comparing with other realisations that these are just a statistical fluctuation in the final posterior, while the tightening of the constraints with number of events is observed repeatedly. Results from the $L_{\text{box}} = 1600$ Mpc/h box.

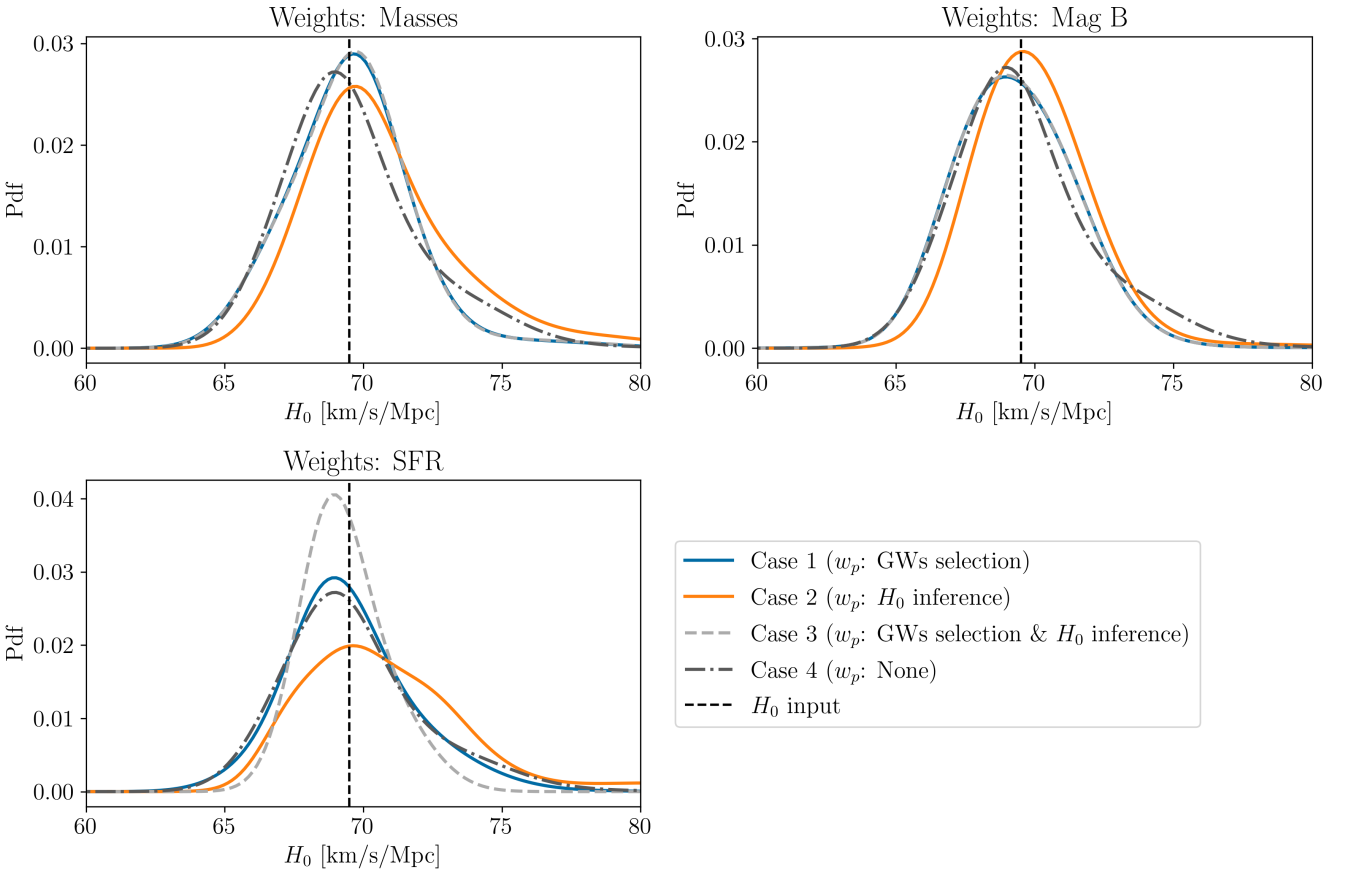


Figure 13. Result of weighted inference for $N_r = 15$ realisations and $N_c = 100$ events from the $L_{\text{box}} = 1600$ Mpc/h box. We test the effects of three physical weights (modeled as described in section 2.6.2). For each weight, we compare four cases: 1) use of weights only at the GW host selection phase; 2) use of weights only at the H_0 posterior calculation phase; 3) use of weights in both phases; and 4) no use of weights at all, i.e., no extra information on top of clustering. We observe that the presence of weights in the mass and B magnitude cases do not offer any advantage, showing that clustering yields the most important information. Only in the case of SFR, the presence of weights does have a noticeable effect, signifying their potential importance when used in dark sirens studies. Finally, it seems the presence of clustering contributes to the absence of any bias, when weights are used in a non-consistent way, as in cases 1 and 2. For more details see main text.

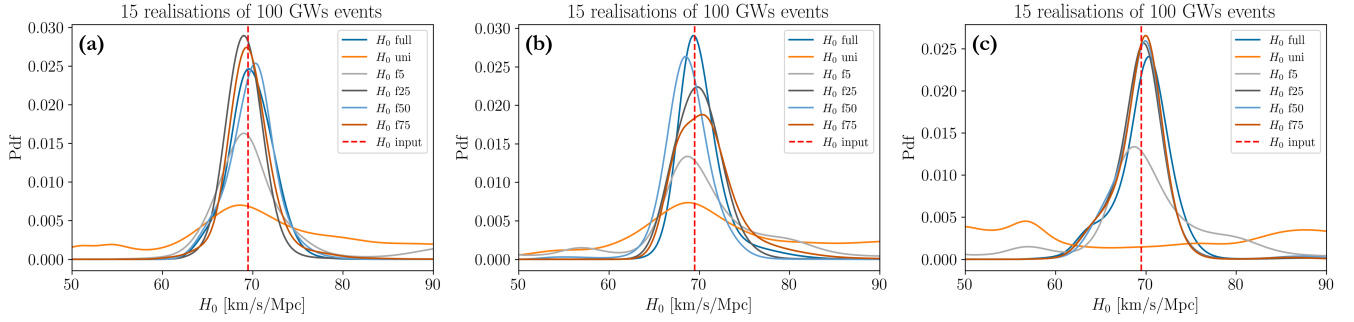


Figure 14. We compare the effects of catalogue incompleteness in three different scenarios: (a) corresponds to the case that new GW events and new catalogues are drawn for each realisation; (b) corresponds to the case that new GW events are drawn for each realisation, but the catalogue is only drawn once and then kept fixed across realisations; and (c) corresponds to the case where the set of GW events are taken from the complete (full) catalogue and used in all the incomplete ones, which are kept fixed. In (a)-(c), we compare the posteriors computed from $N_c = 100$ events averaged over $N_r = 15$ realisations, between the complete/clustered (full) catalogue, the uniform one and the incomplete catalogues of increasing completeness from $f = 5\%$ till $f = 75\%$. We observe that the uniform catalogue and the almost uniform catalogue ($f = 5\%$) are consistently outperformed by the catalogues with increased clustering presence. We generally observe the expected behaviour, with improved inference for increased completeness. Events are taken from the $L_{\text{box}} = 1600$ Mpc/h box. For more details see main text.

(ii) *Case 2:* Opposite of *Case 1*, we use physical weights when calculating H_0 , but do not use them when actually choosing the host of the GW source.

(iii) *Case 3:* Combines *Case 1* and *Case 2* above, and leads to a consistent procedure where the same weights are used for GW source selection and when estimating H_0 .

(iv) *Case 4:* No physical weights. Only geometric information of the galaxies (distances, sky localisation) is used in both GW host selection and H_0 inference.

We note that in all cases geometric weights are used, i.e. are part of the GW likelihood (section 2.6.3). Moreover, although the first two cases are not self-consistent, they are used to investigate possible biases in the method. Finally, observe that although “Case 4” does not impose any explicit weights, the number of low-mass galaxies is bigger than high-mass galaxies due to their formation (recall Fig. 1). As a result, they are preferentially selected in a random draw. However, this is also the case in a realistic scenario with equal prior weights to all galaxies, hence this is not introducing any inconsistency in the “no physical weights” analysis.

In general, we see that the presence of weights does not significantly change our H_0 posteriors, with the exception of weighting by SFR which seems to lead to tighter constraints in the self-consistent analysis of *Case 3*. Furthermore, we observe that the non-symmetrical presence of weights does not appear to lead to biased results in our case (but see also (Hanselman et al. 2025)), and this could be attributed to the presence of clustering having the most significant contribution to the analysis. The latter conclusion is reinforced by the work of (VanWyngarden et al. 2025), who studied the effects of physical weights in clustered catalogues and concluded that in some cases even 1% complete catalogues could lead to unbiased H_0 estimates. This result qualitatively agrees with our conclusions, with some quantitative variations due to different choices of opening angles and luminosity distance uncertainties.

3.2.3 Effects of completeness

We study completeness effects in Figure 14. The Pdfs correspond to $N_c = 100$ GW events, averaged over $N_r = 15$ realisations from the $L_{\text{box}} = 1600$ Mpc/h box. The different Figures 14 (a)-(c) are

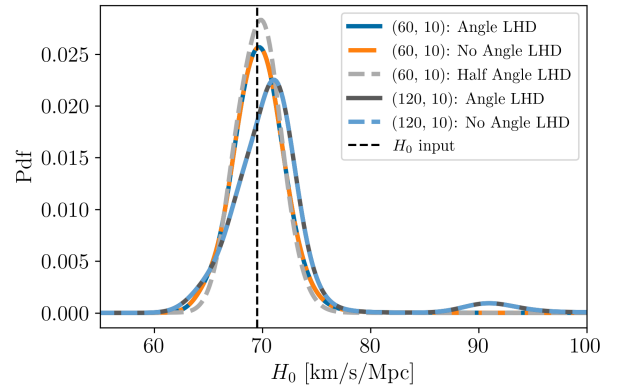


Figure 15. H_0 posteriors for complete catalogues, with and without angle weights (section 2.6.2) in the likelihood. We compare two cases of observational errors ($\Delta\Omega, 100 \cdot A$). We find negligible differences in the final pdfs, regardless of the inclusion of weights. This could be a combination of the smallness of the cones’ opening angle (relatively small $\Delta\Omega$) and of the importance of clustering. We test this assumption with an “artificial boost” of the weight resolution inside the cone - see main text for details, section 3.2.5 - which indeed leads to a visible improvement (in the grey, dashed line). Results are shown for inference of $N_c = 100$ events, averaged over $N_r = 15$ realisations, from the $L_{\text{box}} = 1600$ Mpc/h box.

produced using different completeness scenarios in order to study potential systematics, and we explain the three different cases below:

(i) *New GWs, New Catalogues* (Fiducial): In this scenario, for each realisation we create new incomplete catalogues, i.e., we produce a new uniform box, and randomly draw galaxies from there (New Catalogues). Moreover, when running the inference on a specific catalogue, we draw new GW events from the galaxies of each catalogue (New GWs). This is the fiducial technique used when running multiple realisations. Case (a) in Figure 14.

(ii) *New GWs, Fixed Catalogues:* Similar to the above, but now the incomplete catalogues are fixed, i.e., we draw galaxies from the uniform box only once to complete the catalogues and then these remain the same for all realisations (Fixed Catalogues). Of course, for each realisation, we draw new (random) GW events, unique for each catalogue (New GWs). Case (b) in Figure 14.

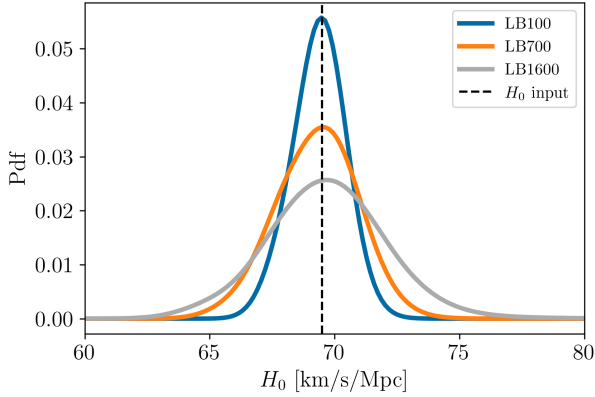


Figure 16. H_0 posteriors for complete catalogues for $N_C = 100$ events, averaged over $N_r = 15$ realisations. We compare runs from the three large particle number boxes $L_{\text{box}} = 100, 700 \text{ \& } 1600$ Mpc/h. GW events from much closer provide more than twice the precision on H_0 ($\sigma_{\text{LB1600}}/\sigma_{\text{LB100}} \sim 2.3$).

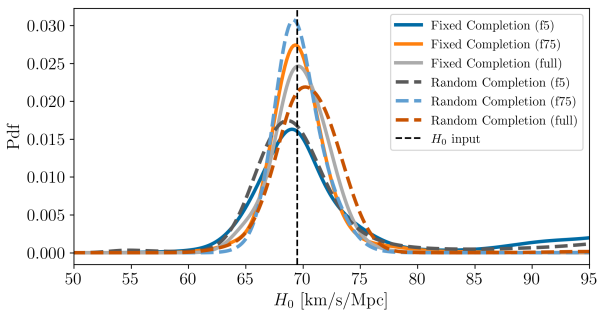


Figure 17. H_0 posteriors for two different completion methods - “fixed” (fiducial, solid lines) and “random” (dashed lines) - for a $f = 5\%, 75\%$ and 100% (full) catalogues, for $N_C = 100$ events, averaged over $N_r = 15$ realisations, from the $L_{\text{box}} = 1600$ Mpc/h box. For the differences on completion methods, we refer to section 3.2.7. We observe that the random completion does not lead to any significant bias, but could lead to inflated posteriors of incomplete catalogues, because this sampling method results in a galaxy distribution with increased clustering.

(iii) *Fixed GWs, Fixed Catalogues:* In this run, the incomplete catalogues are only created once, exactly as the case above (Fixed Catalogues). In addition, here we also keep the GW fixed, in the sense that their coordinates are selected from the clustered (complete) catalogue and then kept the same for all the other (incomplete) catalogues. In other words, for each realisation, the new GW events are chosen from the complete catalogue, and then the same events, i.e. cone positions/sizes, are used in the incomplete catalogues (Fixed GWs). Case (c) in Figure 14.

Irrespective of the method, we draw several general conclusions:

- The uniform catalogue performs consistently worse. This is expected, as it does not include any clustering.
- Increasing the catalogue completeness leads to tighter constraints.
- We observe some variation in terms of which catalogue performs best. A part of this could be explained from the different realisation procedures explored in this section, although the most important factor is the presence of increased clustering in the more

complete catalogues, i.e., we have GW events in sky areas where clustering allows tighter H_0 constraints, which dominate the final posterior. Hence, we observe that completeness levels as low as $f = 25\%$ can be statistically equivalent to fully completed catalogues.

We investigate the last point further in Figure 18, where we focus on three catalogues and an increasing number of events. For all, we have $N_r = 15$ realisations. We use a uniform catalogue, a $f = 50\%$ complete catalogue and a complete catalogue. The four different panels (upper and lower) correspond to the different realisation procedures described in this section. Crucially, this analysis strengthens our results on the importance of clustering, since it demonstrates that even with about half of the galaxies missing from the survey, the posteriors converge strongly and are essentially equivalent to those obtained with the fully complete catalogue.

Moreover, to confirm the robustness of our results, we investigate the galaxy catalogues in terms of their clustering power and the sky positions of the galaxies. We show the correlation function (Landy & Szalay 1993) and their angular distribution in Figure 22. As expected, we see increased power in the more complete catalogues. This validates their construction. We discuss this in more detail in Appendix C, where we show that resolution effects are not affecting our main conclusions.

3.2.4 Effects of observational errors

In Figure 19, we study the impact of observational errors (section 2.3) on the final H_0 posteriors. For all cases, we consider $N_C = 100$ GWs events from the complete catalogue from the big box $L_{\text{box}} = 1600$ Mpc/h, averaged over $N_r = 15$ realisations. As a general conclusion, we establish the expected behaviour: smaller observational errors produce tighter constraints. More specifically, we see that for smaller sky localisation errors, $\Delta\Omega \leq 60$ deg. squared, the distance uncertainty plays the more important role, with the Pdfs of $(\Delta\Omega, 100 \cdot A) = (60, 5)$ and $(30, 5)$ being very similar. In parallel, when the cone openings are large, $\Delta\Omega = 120$ deg. squared, the smaller distance uncertainty is not affecting the H_0 Pdf, with $(120, 10)$ and $(120, 5)$ being almost identical.

3.2.5 Effects of angle weights in the likelihood

In Figure 15, we investigate the effect of giving angular weights to the galaxies inside the cones when inferring the Hubble parameter H_0 . In other words, instead of using eq. (18), we use a uniform probability for all angles. We expect the inclusion of this term to improve our inference, however we find that the final Pdfs are very similar: compare the solid lines (with the angle weights) with the dashed lines (without angle weights). We investigated this further, by looking at cones with different opening angles, doubling the observational errors from $\Delta\Omega = 60$ deg. squared to $\Delta\Omega = 120$ deg. squared. We observe no difference between the runs with and without angular weights in either case.

We believe a combination of reasons lead to this behaviour, and all relate to three various key scales: 1) the GWs angular localisation error, which determines the size of the cone and the width of the exponential weight, 2) the typical size of galaxy clusters, and 3) the typical separation between clusters. We analyse them in turn:

Firstly, if the edge of the cone was only one sigma, then the exponential would be pretty flat across the whole cone. However, our cone edges are more than 1.645σ away from the cone centre. At the same time the sky localisation areas we have considered are

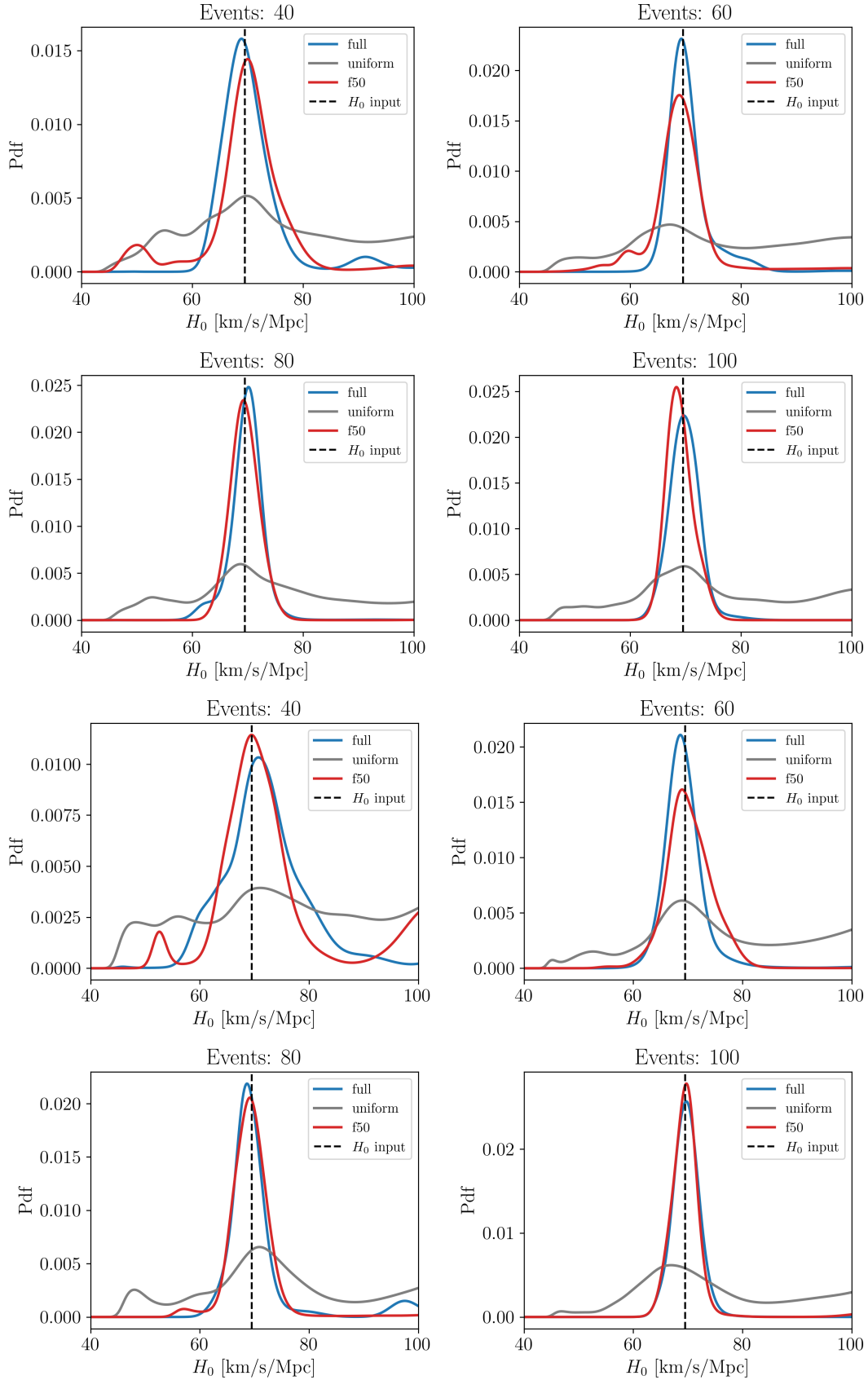


Figure 18. H_0 posteriors comparison, for different number of events, between three catalogues: a complete (full) catalogue, a $f = 50\%$ incomplete catalogue and a uniform catalogue. Top and bottom panels correspond to different realisation scenarios: top 4 figures to fixed catalogues, bottom 4 figures to new catalogues. Results of both panels are similar and show that even a half complete catalogue could lead to similar H_0 Pdfs, due to the presence of clustering. Pdfs averaged over $N_r = 15$ realisations, from the $L_{\text{box}} = 1600$ Mpc/h box. See main text for more details.

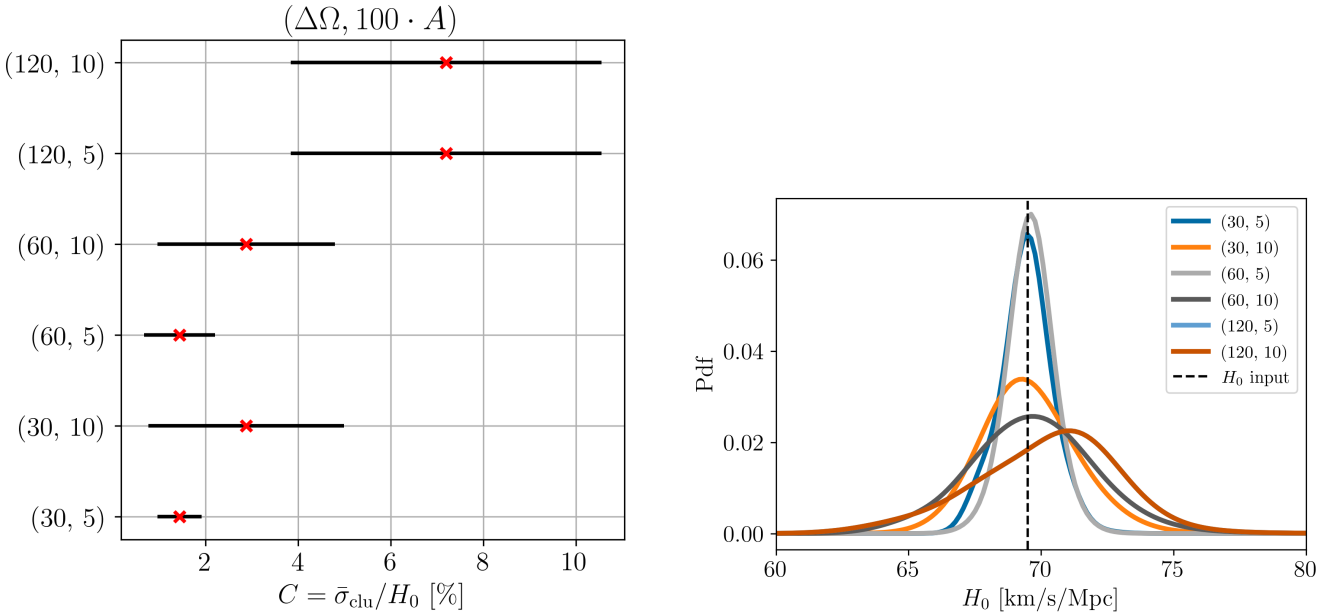


Figure 19. Study of the impact of observational errors ($\Delta\Omega, 100 \cdot A$) on the H_0 Pdfs, for the complete, clustered catalogues. (Left) We show the standard deviation of the Pdfs, normalised to the input $H_0 = 69.5$ km/s/Mpc. For small cone openings, the distance errors play the more important role. For large cone openings, the angular errors dominate. (Right) The full posteriors for the same selection of errors. Note that the (120, 5) posterior is not visible, because it is very similar to the (120, 10) run. Recall that the errors are selected at the beginning of each inference simulation and are kept fixed for all events. Results of inference for $N_c = 100$ events, averaged over $N_r = 15$ realisations, from the $L_{\text{box}} = 1600$ Mpc/h box.

relatively optimistic, so there are no big differences in sky positions - one can see in Fig. 4 the relative small differences between angular weights.

Secondly, if the width of the Gaussian is large compared to the typical cluster size and small compared to the inter-cluster separation the behaviour shown in Fig. 15 might be expected, since the weights are approximately constant across a cluster and the cone does not typically contain more than one cluster in any redshift slice. To check if this is the case, we perform a test run, where we “artificially” reduce the variance of the exponential, i.e. have higher resolution inside the cones, while keeping cone sizes the same. Indeed, this led to a small improvement of the final posterior - see the gray, dashed line.

3.2.6 Effects of different box sizes

In Figure 16, we compare the H_0 posteriors for the three large particle number simulations. We draw $N_c = 100$ GWs events from the complete catalogue and average their posteriors over $N_r = 15$ realisations. The smaller box, with $L_{\text{box}} = 100$ Mpc/h, yields an H_0 Pdf with a width that is half compared to the $L_{\text{box}} = 1600$ Mpc/h box ($\sigma_{L_{\text{box}}1600}/\sigma_{L_{\text{box}}100} \sim 2.3$). This emphasises that closer events would be much more impactful in ‘dark sirens’ analyses.

3.2.7 Effects of completion method

In Figure 17, we compare the effects on H_0 posteriors when completing the incomplete catalogues in two different ways: the “fixed” completion method, described in detail in section 2.7.1 and where the main logic is to introduce galaxies per radial bin, and the “random” method, where we introduce missing galaxies globally. In other words, in the latter procedure, when we calculate the N_{missing} galaxies, we take into account all the galaxies in the observational

sphere. Then we put back N_{missing} galaxies, uniformly over the whole sphere. As a result, this could lead to galaxies being drawn to regions, i.e. radial bins, where no galaxy is missing. We have checked that this procedure changes the expected galaxy distribution: distances further away are not “completed” adequately, and there is stronger clustering, since we introduce galaxies to regions that are not missing any. Although a bias is not observed in the “random” completion method, due to the above reasons, the “fixed” method is the default option throughout.

3.2.8 Effects of H_0 priors

In Figure 20, we compare the effects on H_0 posteriors when assuming different H_0 prior choices: $H_0^{\text{prior}} = [40, 100]$ (fiducial), $H_0^{\text{prior}} = [20, 100]$ (low-asymmetric), and $H_0^{\text{prior}} = [40, 120]$ (high-asymmetric). It is important to note that the prior choices are not affecting only the final inference, but also the cone construction and the range of eligible GW sources. This happens because the cone size takes into account the H_0 prior range, as described in section 2.4 and similarly for the distance threshold of sources, as seen in eq. (26).

As a result, a smaller lower limit allows a more restricted distance range of GW source, i.e. sources are selected closer to the observer, yielding a more precise measurement. To make a fairer comparison and investigate more thoroughly and consistently the effect of the priors, we impose an extra constrain to the fiducial and high-asymmetric runs: we restrict the distance threshold of the GW events to about $L_{\text{box}}/4$, which is roughly the same as the maximum GW source distance recovered in the low-asymmetric case (which uses the fiducial limit $L_{\text{box}}/2$, but the maximum GW distance is much closer due to the prior). In this case, we observe that the final posteriors are equivalent between the three cases, and hence confirm

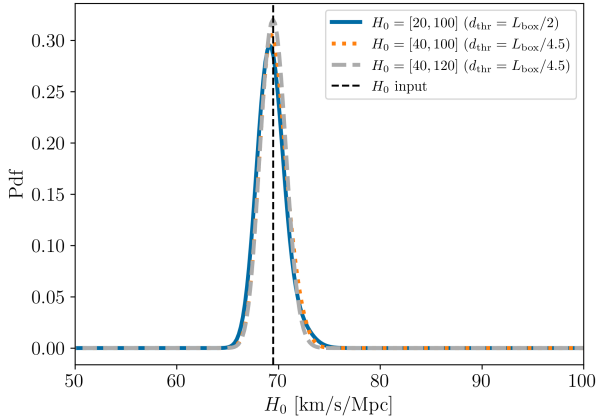


Figure 20. H_0 posteriors for three different H_0 prior choices: the fiducial one $H_0^{\text{prior}} = [40, 100]$ (orange, dotted), the low-asymmetric one $H_0^{\text{prior}} = [20, 100]$ (blue, solid) and the high-asymmetric one $H_0^{\text{prior}} = [40, 120]$ (grey, dashed). The reason for the extra distance constraints is for consistency between all the runs, since a prior change affects also the construction of the catalogue and of the cones (see main text, section 3.2.8 for details). Taking this into account, we observe that all prior runs are equivalent and there are no biases. Results are shown for inference of $N_c = 100$ events, averaged over $N_r = 15$ realisations, from the $L_{\text{box}} = 1600$ Mpc/h box. The normalisation here is defined, so that the Pdfs integrate to 1.

that our results are not prior dependent. Finally, note that the prior choice does not induce any bias.

3.2.9 Convergence studies

In this last section, we cross-check our results by running multiple realisation scenarios. As a reminder, the default number of realisations is $N_r = 15$, and is used throughout unless stated otherwise. This means that for a specific number of events, for example $N_c = 20$, we repeat the analysis N_r times and combine the posteriors.

Figure 21 illustrates the results of our basic test: we use the complete catalogue of the $L_{\text{box}} = 1600$ Mpc/h box and compare the H_0 posteriors for different numbers of GW events and different realisations. In the first case, we confirm that increasing the number of events, even 5-fold, leads to more precise constraints. In the second case, we show that the default number of realisations chosen for our results $N_r = 15$ yields similar H_0 Pdfs with $N_r = 20$ and $N_r = 25$, demonstrating convergence of our analysis.

Moreover, in section 3.2.3 we investigate different completeness realisations to make sure our results are robust with respect to GW event selection and catalogue variability. The results are shown in Figures 14 and 18.

In Figure 14, panels (a)-(c) correspond to the cases (i)-(iii), described in section 3.2.3, respectively. We find that the completeness and GW selection procedures can quantitatively affect the results, but qualitatively they are not very different. The most important difference appears in Figure (c)/case (iii), where both the GW events chosen from the complete catalogue, and also the incomplete catalogues are fixed, however the result is not surprising. Keeping the selected GW events and catalogues consistent across completenesses suppresses the differences arising from random fluctuations due to the event selection. As a result the posteriors look much more similar than in the other cases where these random fluctuations are present.

This panel suggests that $f \geq 25\%$ provides the critical threshold for the completeness levels we have studied, with the quality of the constraint starting to degrade at lower completenesses.

Figure 18 tests cases (i) (top four panels) and (ii) (bottom four panels), demonstrating the qualitative equivalency of the two methods: in both cases, catalogues with clustering perform much better than the uniform one, and even heavily incomplete catalogues could offer similar constraints as complete ones.

4 CONCLUSIONS

In this paper, we have studied the effects of clustering and incompleteness of galaxy surveys, when constraining the Hubble-Lemaître parameter with dark GW sirens. For this, we exploited high-resolution cosmological simulations with realistic structure formation and physical weights. We find that:

- Care is needed to avoid biases in the final H_0 posterior. Based on our simulated analyses, the most important effects come from the geometric characteristics of the problem, i.e., the cone geometry and positions of galaxies. These can be counterbalanced by galaxy weights based on their positions and by selection effects, as well as considering a consistent approach on simulation studies of GW “dark sirens”. Our results confirm the potential problems with biased H_0 inference (Trott & Huterer 2021), and solutions discussed in Gair et al. (2022); Alfradique et al. (2025). As a result, we find that different methods - histogram “stacking” of all H_0 values (section 2.6.1), and the full Bayesian analysis (section 2.6.3) of calculating the H_0 distribution give consistent results, and converge to the input value as the number of observations increases. We do not observe any clear bias in our results.

- The inclusion of physical weights (masses, magnitudes, star formation rates) does not always lead to a significant improvement of the final posterior: weighting by star formation rate seems to have the most significant impact. We caution however that this can be implementation dependent. On the other hand, geometric weights are important and necessary. This reinforces the importance of clustering, which in addition allows for unbiased results even when weights are not applied self-consistently (Figure 13).

- Clustered catalogues improve convergence compared to uniform ones (Figures 14 and 18). This is not true for all methods. In the simplest “stacking” method, the interquartile gap is similar between clustered and uniform catalogues, irrespective of box size and particle numbers. On the other hand, the “Bayesian” analysis shows a clear improvement on the H_0 determination.

- Incomplete catalogues, based on magnitude cuts, perform better than complete uniform ones (Figure 14). This is a direct result of clustering. In some cases, even catalogues only $f = 25\%$ complete, can be competitive with full catalogues. And already from $f = 5\%$ completeness, we see a clear peak in the posterior. We find that these results are robust against different realisation scenarios.

- In terms of observational errors, we find that the angle weights in the likelihood play a secondary role, at least for the cone geometries we consider (Figure 15). Moreover, for small cone openings ($\Delta\Omega < 120$ deg. squared), we showed that the distance errors A , influence strongly the tightness of our posteriors, while for larger openings ($\Delta\Omega \geq 120$ deg. squared) the posteriors are dominated by the angular errors (Figure 19). This behaviour is not unexpected, since in bigger cones the distribution of galaxies “smoothens out”.

- Considering catalogues of different sizes, i.e., different simulation boxes, we confirm that good quality, close-by events are more important than more distant ones. More specifically, the same

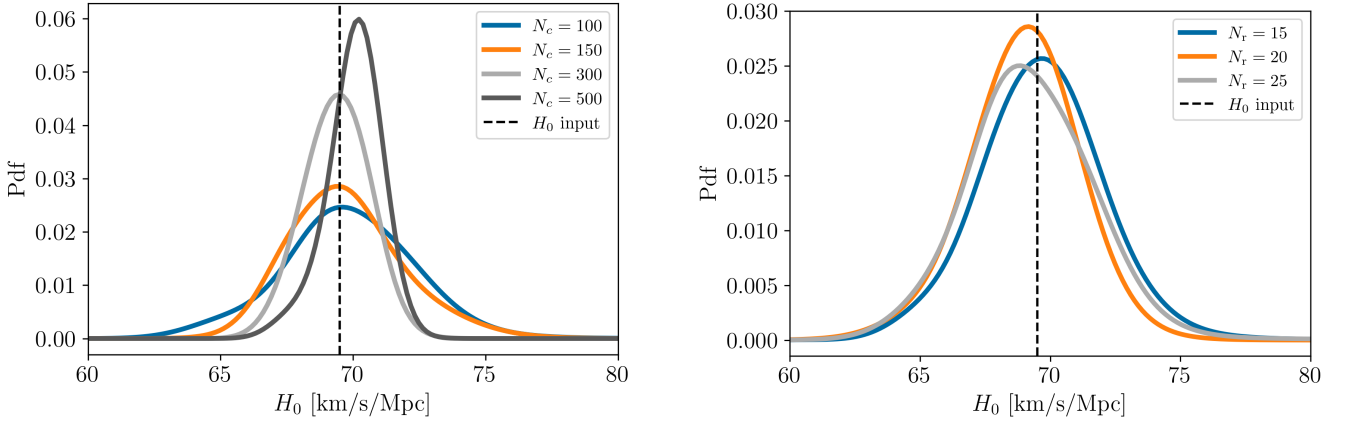


Figure 21. Checking convergence of our inference procedure. (Left) Similar to Figure 12, but reaching $\times 5$ number of GW events. As expected, more observations lead to much more precise results. (Right) We test the impact of the number of realisations N_r , for $N_c = 100$ GW events. We show that for the default number chosen ($N_r = 15$), the pdfs have converged. Results from the $L_{\text{box}} = 1600$ Mpc/h box.

number of events lead to almost double the Pdf width for the larger observing sphere ($\sigma_{L_{1600}}/\sigma_{L_{100}} \sim 2.3$) (Figure 16).

- The most important result of this work demonstrates the power of clustering in real galaxy surveys. Catalogues that globally retain even $f = 5\%$ of the true number of galaxies in the Universe lead to unbiased and informative constraints (Figure 14). Completeness levels of $f = 50\%$ already perform statistically similar to fully complete catalogues (Figure 18). This indicates that a strategy that focusses on improving GW detector sensitivity and minimizing detector downtime, so that the number of GW events is maximized, is more important for “dark siren” cosmology than obtaining more complete galaxy catalogues.

- Finally, we tested the robustness of our analysis with a number of sanity-checks, which it passes successfully: catalogue construction and clustering behaviour (Figure 22, convergence with number of GW events follows an $1/\sqrt{N}$ scaling (Figures 12 and 21), convergence of posteriors with number of realisations (Figure 21) and resolution effects (section C).

ACKNOWLEDGEMENTS

MK would like to thank Konstantinos Migkas for useful discussions during the 15th Hellenic Astronomical Conference, Andrea Incatasciato & Jose Onorbe for helpful discussions concerning the LEGACY simulations, and Tessa Baker for detailed comments in a very early draft of this paper. The authors also thank Konstantin Leyde for the very helpful internal LVK review, and Simone Mastrogiovanni and Maciej Bilicki for useful comments. SK acknowledges funding via STFC Small Grant ST/Y001133/1. For the purpose of open access, the authors have applied a Creative Commons Attribution (CC BY) license to any Author Accepted Manuscript version arising from this submission.

Software: For the analysis, we used Matplotlib (Hunter 2007), NumPy (Oliphant 2006; Van Der Walt et al. 2011), and SciPy (Virtanen et al. 2020).

DATA AVAILABILITY

The data underlying this article will be shared on reasonable request to the corresponding author. The codes to reproduce the results of

this paper, will appear in https://github.com/MariosNT/Gws_DarkSirens_completeness.

REFERENCES

- Abbott B. P., et al., 2017a, *Phys. Rev. Lett.*, **119**, 161101
 Abbott B. P., et al., 2017b, *Nature*, **551**, 85
 Abbott B. P., et al., 2019, *Physical Review X*, **9**, 031040
 Abbott R., et al., 2020, *ApJ*, **896**, L44
 Abbott R., et al., 2021a, *Physical Review X*, **11**, 021053
 Abbott B. P., et al., 2021b, *ApJ*, **909**, 218
 Abbott B. P., et al., 2021c, *ApJ*, **923**, 279
 Abbott R., et al., 2023a, *Physical Review X*, **13**, 041039
 Abbott R., et al., 2023b, *ApJ*, **949**, 76
 Abbott R., et al., 2024, *Phys. Rev. D*, **109**, 022001
 Acernese F., et al., 2015, *Classical and Quantum Gravity*, **32**, 024001
 Acernese F., et al., 2019, *Phys. Rev. Lett.*, **123**, 231108
 Acernese F., et al., 2023, *Classical and Quantum Gravity*, **40**, 185006
 Afroz S., Mukherjee S., 2024, *MNRAS*, **534**, 1283
 Aghanim N., et al., 2020, *A&A*, **641**, A6
 Akutsu T., et al., 2021, *Progress of Theoretical and Experimental Physics*, **2021**, 05A101
 Alfradique V., Bom C. R., Castro T., 2025, *arXiv e-prints*, p. [arXiv:2503.18887](https://arxiv.org/abs/2503.18887)
 Amaro-Seoane P., et al., 2017, *arXiv e-prints*, p. [arXiv:1702.00786](https://arxiv.org/abs/1702.00786)
 Barbieri R., Kalomenopoulos M., Gair J., Khochfar S., 2025,
 Behroozi P. S., Wechsler R. H., Wu H.-Y., 2013a, *ApJ*, **762**, 109
 Behroozi P. S., Wechsler R. H., Conroy C., 2013b, *ApJ*, **770**, 57
 Beirnaert F., Ghosh A., Dálya G., 2025, *arXiv e-prints*, p. [arXiv:2505.14077](https://arxiv.org/abs/2505.14077)
 Bera S., Rana D., More S., Bose S., 2020, *ApJ*, **902**, 79
 Branchesi M., et al., 2023, *J. Cosmology Astropart. Phys.*, **2023**, 068
 Buikema A., et al., 2020, *Phys. Rev. D*, **102**, 062003
 Capote E., et al., 2025, *Phys. Rev. D*, **111**, 062002
 Chen A., 2025, *arXiv e-prints*, p. [arXiv:2505.12678](https://arxiv.org/abs/2505.12678)
 Chen H.-Y., Fishbach M., Holz D. E., 2018, *Nature*, **562**, 545
 Chen H.-Y., Ezquiaga J. M., Gupta I., 2024, *Classical and Quantum Gravity*, **41**, 125004
 Cigarrán Díaz C., Mukherjee S., 2022, *MNRAS*, **511**, 2782
 Cross-Parkin M. L., Howlett C., Davis T. M., Khetan N., 2025, *arXiv e-prints*, p. [arXiv:2502.17747](https://arxiv.org/abs/2502.17747)
 Cuceu A., Farr J., Lemos P., Font-Ribera A., 2019, *J. Cosmology Astropart. Phys.*, **2019**
 DESI Collaboration et al., 2016, *arXiv e-prints*, p. [arXiv:1611.00036](https://arxiv.org/abs/1611.00036)
 Dalang C., Baker T., 2024, *J. Cosmology Astropart. Phys.*, **2024**, 024

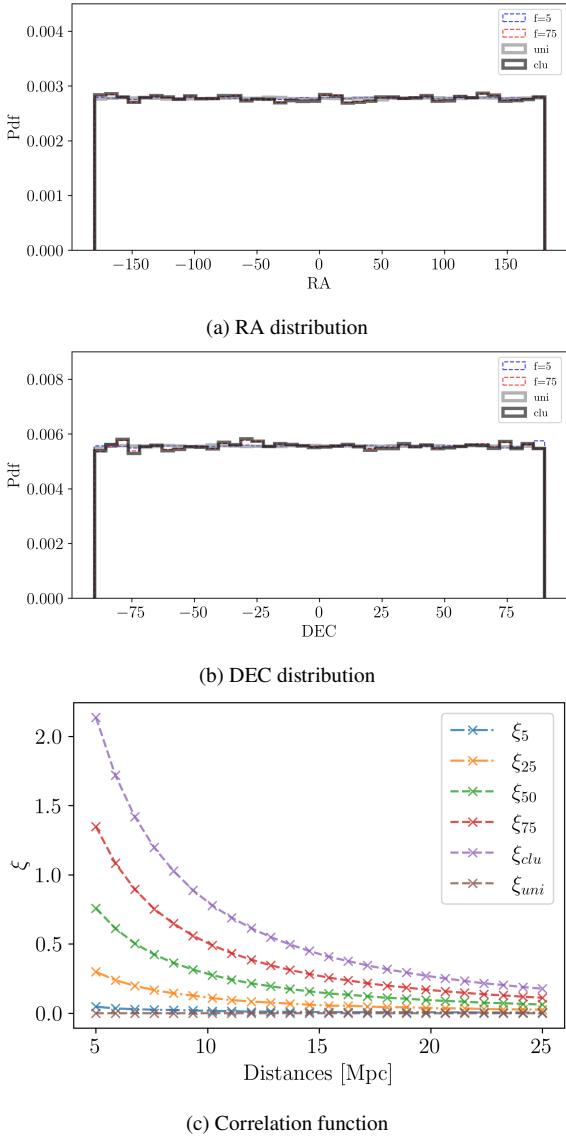


Figure 22. $L = 1600 \text{ Mpc/h}$: Sanity checks for our completion procedure: (a)-(b) the angular distribution of the galaxies in each catalogue - the more clustered the catalogue, the more features we see: the uniform catalogue here is almost flat, with the 5% (blue, dashed) following it very closely; (c) the correlation function of each catalogue. As expected, the clustering increases as we increase the completeness of the catalogue. Note that the 5% catalogue is almost identical to the uniform one. For DEC, the cosine distribution has been transformed to uniform, for easier comparison.

Dalang C., Fiorini B., Baker T., 2024, *arXiv e-prints*, p. [arXiv:2410.03275](#)
Dálya G., et al., 2018, *MNRAS*, 479, 2374
Dálya G., et al., 2022, *MNRAS*, 514, 1403
Davis T. M., Scrimgeour M. I., 2014, *Monthly Notices of the Royal Astronomical Society*, 442, 1117
Dehghani A., Kim J. L., Hosseini D. S., Krolewski A., Mukherjee S., Geshnizjani G., 2025, *J. Cosmology Astropart. Phys.*, 2025, 056
Del Pozzo W., 2012, *Phys. Rev. D*, 86, 043011
Di Valentino E., et al., 2021, *Classical and Quantum Gravity*, 38, 153001
Ding X., Biesiada M., Zheng X., Liao K., Li Z., Zhu Z.-H., 2019, *J. Cosmology Astropart. Phys.*, 2019, 033
Ducoin J.-G., Corre D., Leroy N., Le Floch E., 2020, *MNRAS*, 492, 4768
Dunlop J. S., 2012, in *The First Galaxies*. Springer Berlin Heidelberg, pp 223–292
Evans M., et al., 2021, *arXiv e-prints*, p. [arXiv:2109.09882](#)

Ferri J., Tashiro I. L., Abramo L. R., Matos I., Quartin M., Sturani R., 2025, *J. Cosmology Astropart. Phys.*, 2025, 008
Finke A., Foffa S., Iacovelli F., Maggiore M., Mancarella M., 2021, *J. Cosmology Astropart. Phys.*, 2021, 026
Fishbach M., et al., 2019, *ApJ*, 871, L13
Freedman W. L., 2021, *ApJ*, 919, 16
Freedman W. L., Madore B. F., 2010, *ARA&A*, 48, 673
Friedmann A., 1922, *Zeitschrift fur Physik*, 10, 377
Gair J. R., et al., 2022, *arXiv e-prints*, p. [arXiv:2212.08694](#)
Ghosh T., More S., Bera S., Bose S., 2024, in *32nd General Assembly International Union (IAUGA 2024)*. p. 1303 ([arXiv:2312.16305](#)), [doi:10.48550/arXiv.2312.16305](#)
Girelli G., Pozzetti L., Bolzonella M., Giocoli C., Marulli F., Baldi M., 2020, *A&A*, 634, A135
Gray R., et al., 2020, *Phys. Rev. D*, 101, 122001
Gray R., et al., 2023, *J. Cosmology Astropart. Phys.*, 2023, 023
H0DN Collaboration et al., 2025, *arXiv e-prints*, p. [arXiv:2510.23823](#)
Hanselman A. G., Vijaykumar A., Fishbach M., Holz D. E., 2025, *ApJ*, 979, 9
Hinshaw G., et al., 2013, *ApJS*, 208, 19
Holz D. E., Hughes S. A., 2005, *ApJ*, 629, 15
Hotokezaka K., Nakar E., Gottlieb O., Nissanke S., Masuda K., Hallinan G., Mooley K. P., Deller A. T., 2019, *Nature Astronomy*, 3, 940
Hubble E., 1929, *Proceedings of the National Academy of Science*, 15, 168
Hunter J. D., 2007, *Computing in Science & Engineering*, 9, 90
Jackson N., 2015, *Living Reviews in Relativity*, 18, 2
LIGO Scientific Collaboration et al., 2015, *Classical and Quantum Gravity*, 32, 074001
Landy S. D., Szalay A. S., 1993, *ApJ*, 412, 64
Leandro H., Marra V., Sturani R., 2022, *Phys. Rev. D*, 105, 023523
Lemaître G., 1931, *MNRAS*, 91, 483
Leyde K., Baker T., Enzi W., 2024, *J. Cosmology Astropart. Phys.*, 2024, 013
Leyde K., Baker T., Enzi W., 2025, *arXiv e-prints*, p. [arXiv:2507.12171](#)
MacLeod C. L., Hogan C. J., 2008, *Phys. Rev. D*, 77, 043512
Maggiore M., et al., 2020, *Journal of Cosmology and Astroparticle Physics*, p. 050
Marinacci F., et al., 2018, *MNRAS*, 480, 5113
Mastrogiovanni S., et al., 2021, *Phys. Rev. D*, 104, 062009
Mastrogiovanni S., et al., 2023, *Phys. Rev. D*, 108, 042002
McGibbon R. J., Khochfar S., 2022, *MNRAS*, 513, 5423
Meriot R., Khochfar S., Oñorbe J., Smith B., 2022, *MNRAS*, 512, 27
Messenger C., Read J., 2012, *Phys. Rev. Lett.*, 108, 091101
Messenger C., Takami K., Gossan S., Rezzolla L., Sathyaprakash B. S., 2014, *Physical Review X*, 4, 041004
Moster B. P., Somerville R. S., Maulbetsch C., van den Bosch F. C., Macciò A. V., Naab T., Oser L., 2010, *ApJ*, 710, 903
Moster B. P., Naab T., White S. D. M., 2013, *MNRAS*, 428, 3121
Mukherjee S., Wandelt B. D., Silk J., 2020, *MNRAS*, 494, 1956
Mukherjee S., Wandelt B. D., Nissanke S. M., Silvestri A., 2021, *Phys. Rev. D*, 103, 043520
Mukherjee S., Krolewski A., Wandelt B. D., Silk J., 2024, *ApJ*, 975, 189
Muttoni N., Mangiagli A., Sesana A., Laghi D., Del Pozzo W., Izquierdo-Villalba D., Rosati M., 2022, *Physical Review D*, 105, 043509
Naiman J. P., et al., 2018, *MNRAS*, 477, 1206
Nair R., Bose S., Saini T. D., 2018, *Phys. Rev. D*, 98, 023502
Natarajan P., et al., 2023, *ApJ*, 952, 146
Neistein E., Li C., Khochfar S., Weinmann S. M., Shankar F., Boylan-Kolchin M., 2011, *MNRAS*, 416, 1486
Nelson D., et al., 2018, *MNRAS*, 475, 624
Oliphant T. E., 2006, *A guide to NumPy*. Trelgol Publishing USA
Palmese A., Mastrogiovanni S., 2025, *arXiv e-prints*, p. [arXiv:2502.00239](#)
Palmese A., et al., 2020, *ApJ*, 900, L33
Palmese A., Bom C. R., Mucesh S., Hartley W. G., 2023, *ApJ*, 943, 56
Pillepich A., et al., 2018, *MNRAS*, 475, 648
Poggiani R., 2025, *arXiv e-prints*, p. [arXiv:2506.15410](#)
Reitze D., et al., 2019, in *Bulletin of the American Astronomical Society*. p. 35 ([arXiv:1907.04833](#)), [doi:10.48550/arXiv.1907.04833](#)

- Riess A. G., Casertano S., Yuan W., Macri L. M., Scolnic D., 2019, *ApJ*, 876, 85
- Riess A. G., et al., 2022, *ApJ*, 934, L7
- Schechter P., 1976, *ApJ*, 203, 297
- Schutz B. F., 1986, *Nature*, 323, 310
- Shafieloo A., Keeley R. E., Linder E. V., 2020, *J. Cosmology Astropart. Phys.*, 2020, 019
- Singer L. P., et al., 2016, *ApJ*, 829, L15
- Soares-Santos M., et al., 2019, *ApJ*, 876, L7
- Soni S., et al., 2025, *Classical and Quantum Gravity*, 42, 085016
- Springel V., 2005, *MNRAS*, 364, 1105
- Springel V., et al., 2018, *MNRAS*, 475, 676
- Springel V., Pakmor R., Zier O., Reinecke M., 2021, *MNRAS*, 506, 2871
- Steer I., 2020, *AJ*, 160, 199
- Taylor S. R., Gair J. R., Mandel I., 2012, *Phys. Rev. D*, 85, 023535
- The Dark Energy Survey Collaboration 2005, *arXiv e-prints*, pp astro-ph/0510346
- The LIGO Scientific Collaboration et al., 2025a, *arXiv e-prints*, p. arXiv:2508.18082
- The LIGO Scientific Collaboration et al., 2025b, *arXiv e-prints*, p. arXiv:2508.18083
- The LIGO Scientific Collaboration the Virgo Collaboration the KAGRA Collaboration 2025c, *arXiv e-prints*, p. arXiv:2509.04348
- Tinker J., Kravtsov A. V., Klypin A., Abazajian K., Warren M., Yepes G., Gottlöber S., Holz D. E., 2008, *ApJ*, 688, 709
- Trott E., Huterer D., 2021, *arXiv e-prints*, p. arXiv:2112.00241
- Tse M., et al., 2019, *Phys. Rev. Lett.*, 123, 231107
- Turski C., Bilicki M., Dályá G., Gray R., Ghosh A., 2023, *MNRAS*, 526, 6224
- Turski C., Brozzetti M. L., Dályá G., Punturo M., Ghosh A., 2025, *arXiv e-prints*, p. arXiv:2505.13568
- Van Der Walt S., Colbert S. C., Varoquaux G., 2011, *Computing in Science & Engineering*, 13, 22
- VanWynngarden M., Fishbach M., Vijaykumar A., Guerrero A. G., Holz D. E., 2025, *arXiv e-prints*, p. arXiv:2511.04786
- Virtanen P., et al., 2020, *Nature Methods*, 17, 261
- Weinberg S., 2008, *Cosmology*. Oxford University Press
- Wong K. C., et al., 2020, *MNRAS*, 498, 1420
- Yang X., Mo H. J., van den Bosch F. C., 2003, *MNRAS*, 339, 1057

APPENDIX A: NUMBER OF GALAXIES IN SIMULATIONS

Resolution limitations restrict the number of galaxies in the region of interest compared to the real Universe. We find about an order of magnitude fewer galaxies than in a real survey. This would lead to individual posteriors to be more optimistic than real observations, however the effects of clustering should hold both qualitatively and quantitatively, since they are based on the relative comparison with an identically populated uniform box. This is confirmed by the investigation of resolution effects in Appendix C.

APPENDIX B: CONSISTENCY CHECKS FOR PHYSICAL PARAMETERS

Before using the ML generated magnitudes and the stellar masses from eq. (1), we performed sanity checks to assess their characteristics. We removed the least massive haloes, which cannot be resolved due to resolution limitations and we checked that the maximum stellar mass of the fiducial $L_{\text{box}} = 1600 \text{ Mpc}/h$ box is smaller than $M_* < 10^{12} M_{\odot}$, which is reasonable for galaxies scales. For the SFR and apparent magnitudes, we retained only galaxies which had physical values assigned, e.g. not negative SFRs. Finally, we confirmed that the distributions of K and B bands (note though that

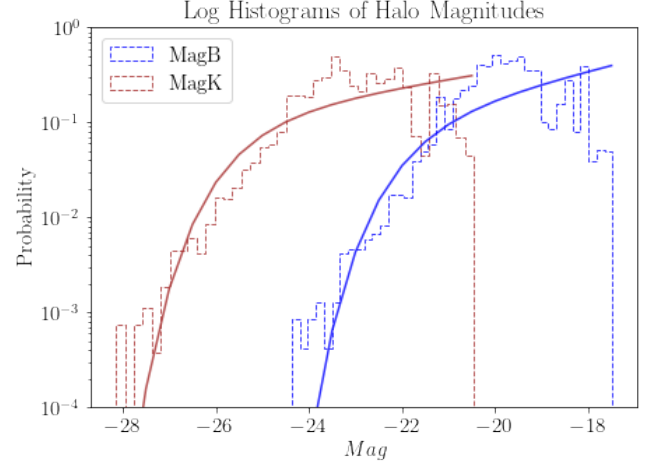


Figure B1. Absolute magnitudes in *B* and *K* bands, approximated by a Schechter magnitude function.

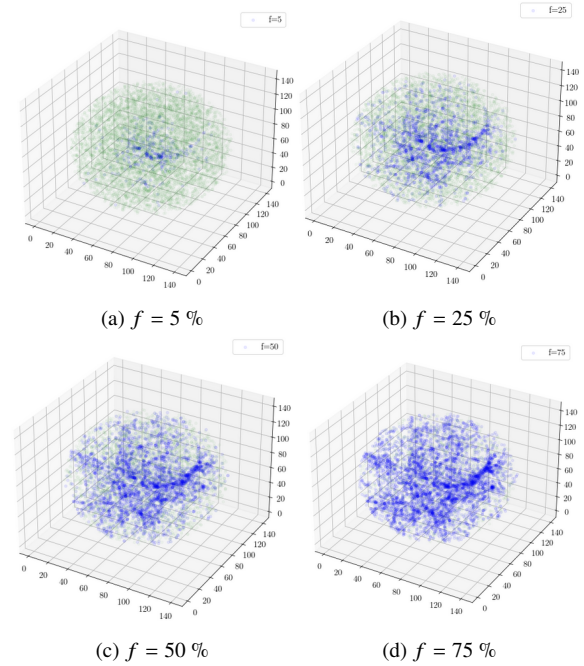


Figure B2. Four spheres with different completeness levels. Green dots correspond to the uniformly distributed points, used to complete the catalogues, while the blue dots are the galaxies that survive the initial magnitude cut. Higher completeness levels preserve more clustering. These boxes correspond to the low particle number simulation of 256^3 particles, in a $100 \text{ Mpc}/h$ size cube for easier visualisation.

only the latter are used in the main text) of the remaining galaxies follow a Schechter magnitude function (Schechter 1976). In Figure B1, we plot such a function, based on (Dunlop 2012, eq. 5), with $(M_*, \alpha) = (-25.5, -1.2)$ and $(M_*, \alpha) = (-22, -1.3)$ for *K* and *B* band respectively.

APPENDIX C: RESOLUTION EFFECTS

To develop our analysis, we have used a low particle number box from the LEGACY suite of cosmological simulations. This test box

has 100Mpc/h length per side, with a resolution of 256^3 particles. Together with the large particle number boxes of different sizes, as described in the main text, this box can be used to investigate any resolution issues of our results. We find that our main results still hold qualitatively in all the boxes.

In Figure B2, we demonstrate how the catalogues of different completeness compare with each other. The blue dots are the clustered galaxies of the original catalogue that survive the magnitude cut, while the green dots correspond to the galaxies that are inserted to complete the catalogue and are drawn from the uniform sample box. In Figure C1, we perform a number of sanity checks to validate our completion procedure: we calculate the angular distributions on the sky of the galaxies for four catalogues (complete, uniform, $f = 5\%$ and $f = 75\%$ completeness) and their correlation function (Landy & Szalay 1993). In all cases, the qualitative behaviour is as expected: the more complete the catalogue, i.e., the higher the clustering, the more features in the angular distribution of galaxies and stronger correlation power (compare with Figure 22).

In Figures C2a and C2b, we present H_0 posteriors for increasing numbers of observations and increasing catalogue completeness in the small box.

This paper has been typeset from a \LaTeX file prepared by the author.

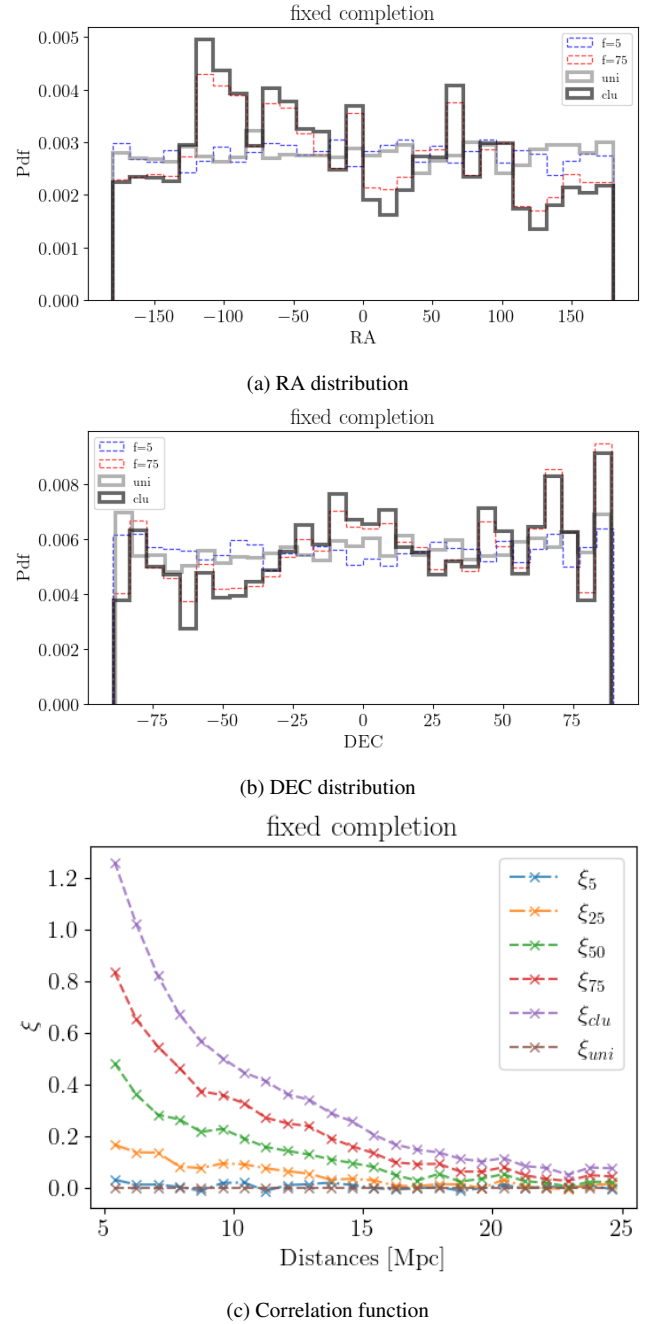
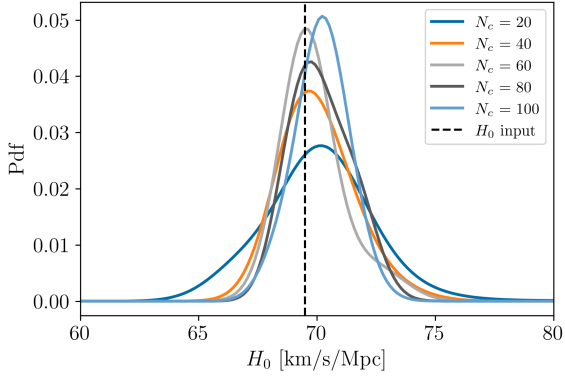
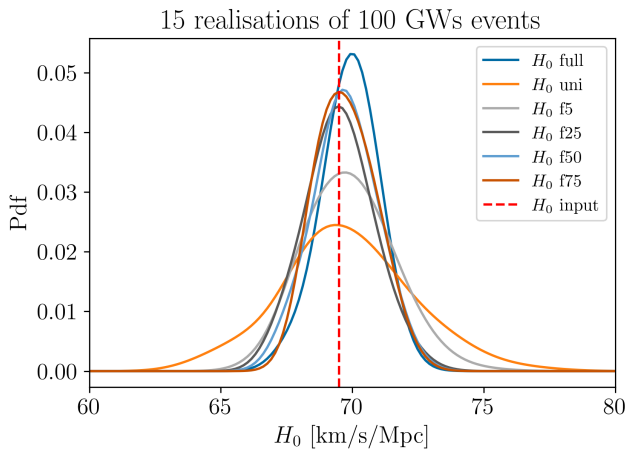


Figure C1. $L = 100 \text{ Mpc/h}$ - small particle number: Sanity checks for our completion procedure: (a)-(b) the angular distribution of the galaxies in each catalogue - the more clustered the catalogue, the more features we see; and (c) the correlation function of each catalogue. As expected, the clustering increases as we increase the completeness of the catalogue. For DEC, the cosine distribution has been transformed to uniform, for easier comparison.



(a) Investigating convergence with number of events



(b) Investigating completeness

Figure C2. H_0 posteriors in the small, small particle number, test box: (a) shows the convergence of the posteriors with the number of events; and (b) compares the posterior for $N_c = 100$ events from different completeness catalogues. For both cases, the qualitative behaviour is similar to the one shown in the large particle number boxes (compare specifically with the H_0 posterior of ‘LB100’ in Figure 16): more events lead to tighter constraints (although we observe a small variability there) and likewise for more complete catalogues. For both figures the results are the average over $N_r = 15$ realisations.